AGU PUBLICATIONS

JGR

Journal of Geophysical Research: Oceans

RESEARCH ARTICLE

10.1002/2015JC011349

Key Points:
- Cumulative FSD in the MIZ has gradual shallower slope toward smaller floes
- Orientation of long leads correlates with wind direction
- Spacing of short leads correlates with wavelength

Correspondence to:
H. H. Shen,
hhshen@clarkson.edu

Citation:
Wang, Y., B. Holt, W. Erick Rogers, J. Thomson, and H. H. Shen (2016), Wind and wave influences on sea ice floe size and leads in the Beaufort and Chukchi Seas during the summer-fall transition 2014, *J. Geophys. Res. Oceans*, *121*, 1502–1525, doi:10.1002/2015JC011349.

Received 26 SEP 2015
Accepted 25 JAN 2016
Accepted article online 26 JAN 2016
Published online 20 FEB 2016

Wind and wave influences on sea ice floe size and leads in the Beaufort and Chukchi Seas during the summer-fall transition 2014

Yu Wang[1], Benjamin Holt[2], W. Erick Rogers[3], Jim Thomson[4], and Hayley H. Shen[5]

[1]Physical Oceanography Laboratory, Department of Oceanography, Ocean University of China, Qingdao, China, [2]Jet Propulsion Laboratory, California Institute of Technology, Pasadena, California, USA, [3]Naval Research Laboratory, Stennis Space Center, Mississippi, USA, [4]Applied Physics Laboratory, Department of Civil and Environmental Engineering, University of Washington, Seattle, Washington, USA, [5]Department of Civil and Environmental Engineering, Clarkson University, Potsdam, New York, USA

Abstract Sea ice floe size distribution and lead properties in the Beaufort and Chukchi Seas are studied in the summer-fall transition 2014 to examine the impact on the sea ice cover from storms and surface waves. Floe size distributions are analyzed from MEDEA, Landsat8, and RADARSAT-2 imagery, with a resolution span of 1–100 m. Landsat8 imagery is also used to identify the orientation and spacing of leads. The study period centers around three large wave events during August–September 2014 identified by SWIFT buoys and WAVEWATCH III® model data. The range of floe sizes from different resolutions provides the overall distribution across a wide range of ice properties and estimated thickness. All cumulative floe size distribution curves show a gradual bending toward shallower slopes for smaller floe sizes. The overall slopes in the cumulative floe size distribution curves from Landsat8 images are lower than, while those from RADARSAT-2 are similar to, previously reported results in the same region and seasonal period. The MEDEA floe size distributions appeared to be sensitive to the passage of storms. Lead orientations, regardless of length, correlate slightly better with the peak wave direction than with the mean wave direction. Their correlation with the geostrophic wind is stronger than with the surface wind. The spacing between shorter leads correlates well with the local incoming surface wavelengths, obtained from the model peak wave frequency. The information derived shows promise for a coordinated multisensor study of storm effects in the Arctic marginal ice zone.

1. Introduction

The continuing reduction of the minimum summer Arctic sea ice extent [*Stroeve et al*., 2012] and shifts in the Arctic atmospheric circulation [*Overland et al*., 2012] have led to speculations of an ice-free summer [*Overland and Wang*, 2013] and to studies on the relationship of the reduced ice cover with recent storm activity including the great cyclone in August 2012 [*Simmonds and Keay*, 2009; *Simmonds and Rudeva*, 2012; *Parkinson and Comiso*, 2013; *Zhang et al*., 2013]. Relating to the reduction of ice, the increase in open water exposes the ocean to more heating and increases fetch and subsequent generation of great waves [*Thomson and Rogers*, 2014]. The compound effect of increasing winds and waves on the already thinner ice covers [*Kwok et al*., 2009] can accelerate the overall ice cover decline and melt rate, by an increase in mechanical fracturing and reduction in floe size, which in turn exposes more ice surface area to be in contact with the warming ocean [*Steele et al*., 2008]. How storms affect the sea ice cover has become a key question of the changing Arctic climate system.

Storms alter the ice cover by the associated wind and wave forcing. This phenomenon is more thoroughly studied in the Antarctic than in the Arctic where the sea ice cover is continuously exposed to incoming forcing from storms. Waves are known to fracture the ice cover [*Squire*, 1984; *Liu and Mollo-Christensen*, 1988] and in turn are scattered [*Wadhams et al*., 1986] and attenuated [*Wadhams et al*., 1988; *Kohout et al*., 2014] by the resulting ice field. Waves and wind also directly impact ice formation, leading to the formation of frazil, grease, and pancake ice that occurs during the more turbulent conditions [e.g., *Wadhams*, 2000]. The change of floe-size distribution (FSD) due to waves and wind may be indicative of these interactive

processes, which have yet to be incorporated into the new generation of coupled sea ice-wave models. These models include ice concentration and thickness distribution but do not yet incorporate waves or floe size information. A significant amount of theoretical work has been carried out that provides models for wave-induced fracturing and the resulting floe size [e.g., *Williams et al*., 2013a, and references therein]. Likewise, theories have also been developed that consider ice effects on wave modeling (see the review by *Squire* [2007] and a recent study of *Williams et al*. [2013b]). However, validation and parameterization of these theories present significant observational challenges.

Starting from *Rothrock and Thorndike* [1984], there have been a number of FSD studies in polar and subpolar regions [e.g., *Toyota et al*., 2006, 2011, and references therein]. Closely related to ice floe formation is the formation of leads, which are defined as large fractures within a frozen ice cover. In the fall period, floes in the MIZ that have survived through the summer melt will become aggregated together by new ice growth, forming a more expansive and continuous ice cover. Wind and waves then may cause fracturing of this still relatively thin, recently aggregated ice cover into quasi-linear leads. This process of melt, growth, aggregation, and fracturing fluctuates during the fall season. Leads are formed everywhere, but more so near the ice edge than in the central Arctic [*Wadhams*, 2000]. In the pack ice zone, leads have been identified to be closely related to the internal stress field [*Cunningham et al*., 1994; *Richter-Menge et al*., 2002]. Despite their small areal fraction over the entire Arctic ice cover, they are intense heat vents in winter [*Maykut*, 1986] and they may precede the formation of FSD in summer. *Weeks* [2010] summarized key issues concerning leads studies in his book. Recent studies by *Bröhan and Kaleschke* [2014] and *Willmes and Heinemann* [2015] gave a summary of the lead statistics in the entire Arctic. The former covered a 9 year period of 2002–2011. Both FSD and leads are important to ice cover morphology and wind/wave forcing in the marginal ice zone (MIZ) between the pack ice and the open ocean.

The fast evolving Arctic climatology has prompted focused studies that integrate field, remote sensing, and modeling with available contemporary tools to understand the physics of this complex system (e.g., http://www.apl.washington.edu/project/project.php?id=miz and http://www.apl.washington.edu/project/project.php?id=arctic_sea_state). Making use of the available data related to these field programs, we perform a much smaller scope exercise using integrated satellite ice cover imagery, together with wind and wave data from in situ and modeling results, to sense the level of information that can be obtained. We focus on remote sensing images at different scales to measure the ice cover morphology defined by two parameters: the FSD and lead characteristics. We then evaluate the effect of wind and wave conditions on these parameters using wind data from NCEP and wave data from a wave hindcast model. Unlike a coordinated field program, our data set is not ideal in that the imagery and in situ wind and wave data are not well collocated or coordinated. Despite such deficiencies, best effort is utilized to envision the amount of future knowledge that will be derived from an integrated and coordinated field study.

In what follows, section 2 introduces the data sets used in this study. Section 3 provides the relevant wind and wave data from in situ and model simulations, used to identify the periods of high winds and waves during August and September 2014. Section 4 presents the image analysis from multiple types of satellite data within a region of the Beaufort and Chukchi Seas. We first derive floe size and examine the resulting distribution statistics. Then we examine satellite data in a period when semicontinuous ice sheets with distributed leads were present, from which we determine the lead orientation and spacing. We discuss these findings in section 5 and conclude our study in section 6.

2. Data Sets and Methods

In the last two decades, remote sensing tools, in situ measurements, and meteorological-oceanography modeling capabilities have all greatly improved. In addition to wind data, we now have direct measurements of waves using buoys in the Arctic, improved wave model products for the Arctic Ocean, and expanding collections of high-resolution remote sensing imagery.

Direct observations of the Arctic Ocean via different remote sensing tools are becoming more available [*Lubin and Massom*, 2006; http://www.remss.com/missions, http://en.wikipedia.org/wiki/Remote_sensing_satellite_and_data_overview]. These remote sensing tools cover a wide range of spatial resolution. In addition, a small set of optical imagery at 1 m resolution has been released for scientific use [*Kwok*, 2014]. Limitations in the past due to resolution for determining the ice FSD in the small floe ranges are greatly relaxed.

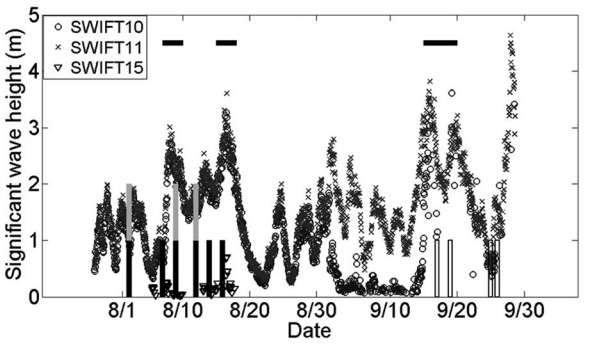

Figure 1. Time series of significant wave height from SWIFT buoy data and dates of satellite images collected for floe size analysis. The horizontal black lines represent the duration of the wave event. The vertical bars represent the dates of images: black = MEDEA, gray = RADARSAT-2, and hollow = Landsat8.

In the present study, we present observations in the Beaufort/Chukchi Seas bounded by 137°W–170°W longitudes and 72°N–79°N latitudes. Two types of ice morphological parameters are studied: the FSD and lead characteristics in the marginal ice zone, where the continuous ice cover is most exposed to forcing from the open ocean. We use three types of satellite imagery: MEDEA, Landsat8, and RADARSAT-2. Their respective spatial resolutions are 1, 15, and 100 m.

To select periods of our study, we examine an in situ wave data set from a series of drifting SWIFT buoys. These buoys were deployed in late July 2014 as part of the Marginal Ice Zone field program (http://www.apl.washington.edu/project/project.php?id=miz). The buoys were recovered in late September 2014. Measurement details of these buoys are given in *Thomson* [2012]. The wave data processing details can be found in *Herbers et al.* [2012]. All wave data used in this study are publically available at http://apl.uw.edu/swift. Figure 1 shows the time series of the significant wave height. There are three major wave events in August–September 2014. They are 7–10 August, 15–19 August, and 17–21 September, marked by the three horizontal bars over the time series. We thus select these periods to collect available satellite imagery in the chosen study region.

There are only a limited number of MEDEA and RADARSAT-2 images for the study period suitable for the analysis. For the Landsat8 images, we selected only those that are relatively cloud-free. The dates and types of images to be analyzed are superimposed with the buoy wave data in Figure 1. As can be seen, only MEDEA and RADARSAT-2 have some temporal overlap.

In Figure 2a we show the trajectories of the three SWIFT buoys (10, 11, and 15), superimposed with two ice edge locations, one for mid-August and one for mid-September. For August, only the ice edge location is shown. For September, the gray scale shows the ice concentration. The relative locations of the two ice edges give a rough estimate of the ice cover retreat during that period. The ice edge information is obtained from Near-Real-Time DMSP SSM/I-SSMIS Daily Polar Gridded Sea Ice Concentrations [*Maslanik and Stroeve*, 1999] derived from National Snow and Ice Data Center (NSIDC). Following *Worby and Comiso* [2004], the 15% ice concentration contour is defined as the ice edge in the present study. For clarity, MEDEA and RADARSAT-2 images used for FSD in the August period are shown in Figure 2b, with Landsat8 images used for the September period shown in Figure 2c. Figure 2d shows the Landsat8 images used in the leads analysis. In each of these plots, ice edges on three dates close to the time when the images were taken are shown. These contours provide visual estimates of the distance to the ice edge for each image, and the advance/retreat history of the ice edge during the image period.

Because the buoys were not located within satellite image locations, to relate the local wave condition to the ice cover we also use wave model data. *Thomson and Rogers* [2014] demonstrated that WAVEWATCH III® (WW3) results agreed very well with buoy data in open water. Figure 3 shows the WW3 simulation results for SWIFT10 and 11, the longest time record of the buoy data available. Figure 2a indicates that most of the time these buoys were in open water. When in ice-covered regions, the dissipation of wave energy by sea ice needs to be considered. At present there are four options (IC0, IC1, IC2, and IC3) in WW3 to account for ice dissipation. In turn, they use the original partial energy blocking scheme [*Tolman*, 2003], a constant damping rate, the eddy viscosity model [*Liu and Mollo-Christensen*, 1988], or a viscoelastic ice layer model [*Wang and Shen*, 2010]. Comparison of these four options has shown clear differences of the predicted wave condition [*Rogers and Zieger*, 2014]. In this study, we use IC3, the viscoelastic ice layer model, for the ice-covered region. This choice is based on a recent study which compared the four ice models with in situ data obtained in the Southern Ocean and found that IC3 appeared to agree the best with data [*Li et al.*, 2015]. In this study we will use both SWIFT and WW3 data to determine the regional wave conditions surrounding the locations of the ice images.

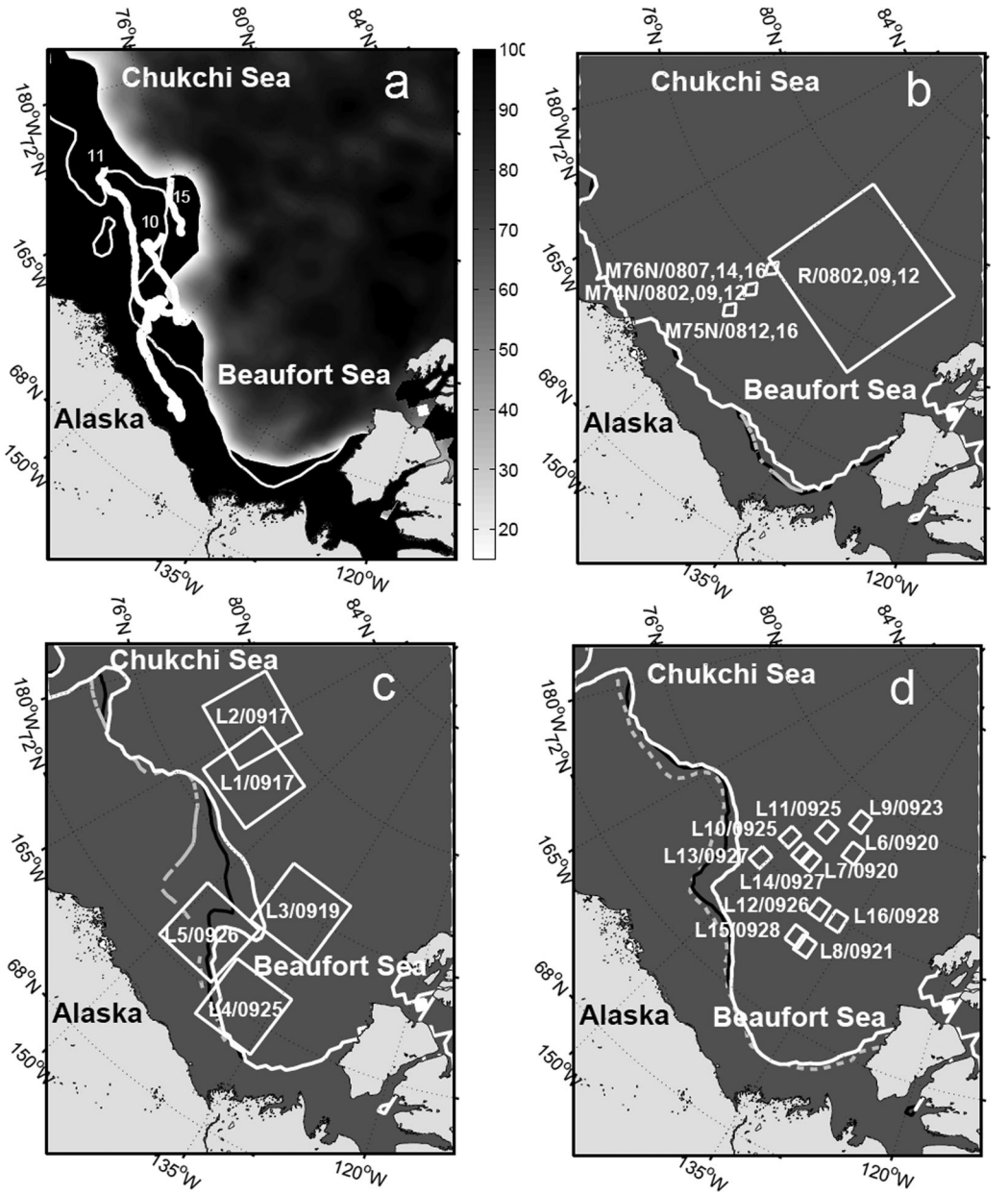

Figure 2. Data map. (a) SWIFT trajectories superimposed with the gray-scale ice concentration on 17 September and the 15% ice concentration on 16 August represented by the thin white contour line; the buoys generally drift west in time with buoy numbers marking their respective end points. (b) The location and dates of all MEDEA and RADARSAT-2 images used for the FSD analysis and the 15% ice concentration contours on 2 August (white), 9 August (black), and 16 August (gray dash). (c) All Landsat8 images used for the FSD analysis and the 15% ice concentration contours on 17 September (white), 19 September (black), and 25 September (gray dash). (d) All Landsat8 images used for lead analysis and the 15% ice concentration contours on 20 September (white), 23 September (black), and 26 September (gray dash). In Figure 2b, the white diamonds indicating MEDEA image locations are larger than their actual frame size, but the white box indicating RADARSAT-2 images is roughly the size of the images. The isolated ice patch outside the 15% contour visible in Figure 2a is also removed here for clarity. In Figure 2c, the Landsat8 polygons roughly correspond to their true frame size. In Figure 2d, the symbols only represent the center locations of the Landsat8 images.

The overall comparison between the buoy data and the simulation results as shown in Figure 3 is reasonable. The correlation coefficient between SWIFT10 and the IC3 model results is 0.82, between SWIFT11 and IC3 is 0.93. But the values of the normalized root-mean-square-difference (NRMSD) calculated as $\sqrt{\sum\left(\frac{X_c-X_m}{X_m}\right)^2/N}$ are very different, in which X_c is the model data, X_m is the measured data, and N is the sample number. The NRMSD between SWIFT11 and IC3 is 0.29, but that between SWIFT10 and IC3 is 2.1. It is obvious that SWIFT11 compared well with the model results over the whole time series, but SWIFT10 did not compare well from 1

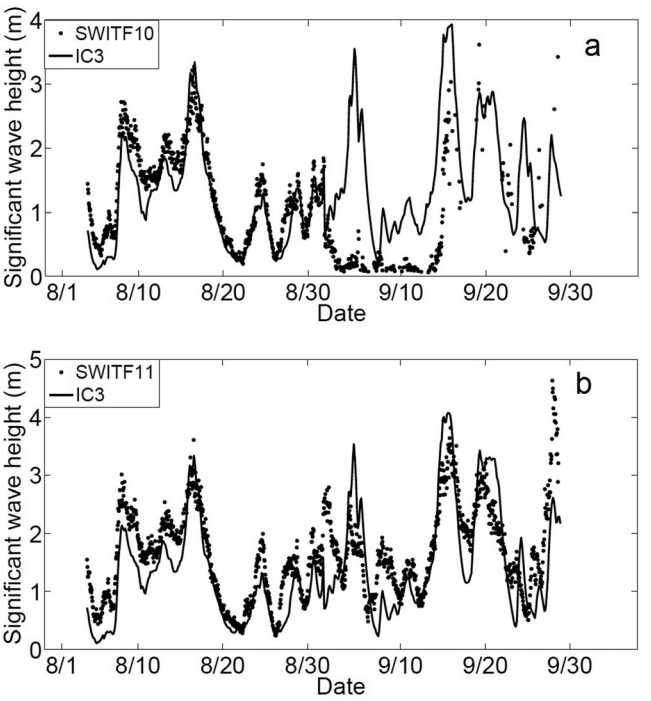

Figure 3. Comparison of (a) SWIFT10 and (b) SWIFT11 data with WW3 model using IC3 with the elastic parameter set at 0 and viscous parameter at 1.

to 15 September. During that period SWIFT10 was surrounded by ice as verified from the record obtained by a camera mounted on the buoy, even though its location was outside the ice edge defined by the 15% ice concentration contour (http://faculty.washington.edu/jmt3rd/SWIFTdata/ArcticOcean/SWIFT10_Sep1_Sep15_Timelapse.mp4).

We now describe the image sources. MEDEA optical imagery first became available in June 2009 when the USGS began to release to the public numerous optical images of Arctic sea ice with 1 m resolution obtained from the National Technical Means (NTM) system. The images are stored in the Global Fiducials Library (GFL) (http://gfl.usgs.gov/) and have various uses for sea ice research including what is described here [*Fetterer and Untersteiner*, 1998; *Kwok*, 2014].

The Landsat program is a series of Earth-observing satellite missions jointly managed by NASA and the U.S. Geological Survey [*Roy et al*., 2014]. The Landsat8 optical images consist of 11 bands including: eight spectral bands with a spatial resolution of 30 m for bands 1–7 and 9, a panchromatic band 8 with a spatial resolution of 15 m, and thermal bands 10 and 11 collected at 100 m resolution. These images are available at http://LandSAT.usgs.gov/Landsat8.php. In our study we use panchromatic band 8 with 15 m resolution.

RADARSAT-2 is a C-band (5.4 GHz) SAR system developed by the Canadian Space Agency (CSA). Different image modes of RADARSAT-2 have a wide range of resolutions from 3 to 100 m. For the time and location of our interest, we utilize three images with a 100 m resolution and a 500 km wide swath. Fortunately, these images are coincident and roughly collocated with the MEDEA images, hence may be used to compare with MEDEA images at a much different scale. These RADARSAT-2 images were collected by the Center for Southeastern Tropical Advanced Remote Sensing (CSTARS) in support of the Marginal Ice Zone program (http://www.apl.washington.edu/project/project.php?id=miz) and made available for use within the related Sea State program (http://www.apl.washington.edu/project/project.php?id=arctic_sea_state).

Examples of the input images used from these sources are shown in Figure 4. From the 1 m resolution MEDEA image individual floes with a broad size range are easily seen. This image was taken on 16 August at 150°W, 76°N. From the NSIDC ice data shown in Figure 2b, this location was roughly 400 km from the ice edge on that day with a local ice concentration >90%. Even at this large distance from the ice edge, the ice cover was quite fragmented. The image size of the Landsat8 was much larger than the MEDEA images. Figure 4b shows an example of the size difference between MEDEA images and Landsat8 images. (Note that the images are neither coincident nor collocated.) The image sizes of the RADARSAT-2 images were even larger, roughly the same as the large white box shown in Figure 2b. As can be seen in Figure 4b, Landsat8 data are subject to cloud cover which prevents useful sea ice analysis. For RADARSAT-2 the issue is clarity or detectability of the floes within the surrounding ice and ocean matrix. Both Landsat8 and RADARSAT-2 images were trimmed before image processing to remove cloudy or difficult regions to utilize. The list of these images with their sources, dates, image location, frame size, resolution, their original image identification label, and their name used in this study are given in the Appendix A.

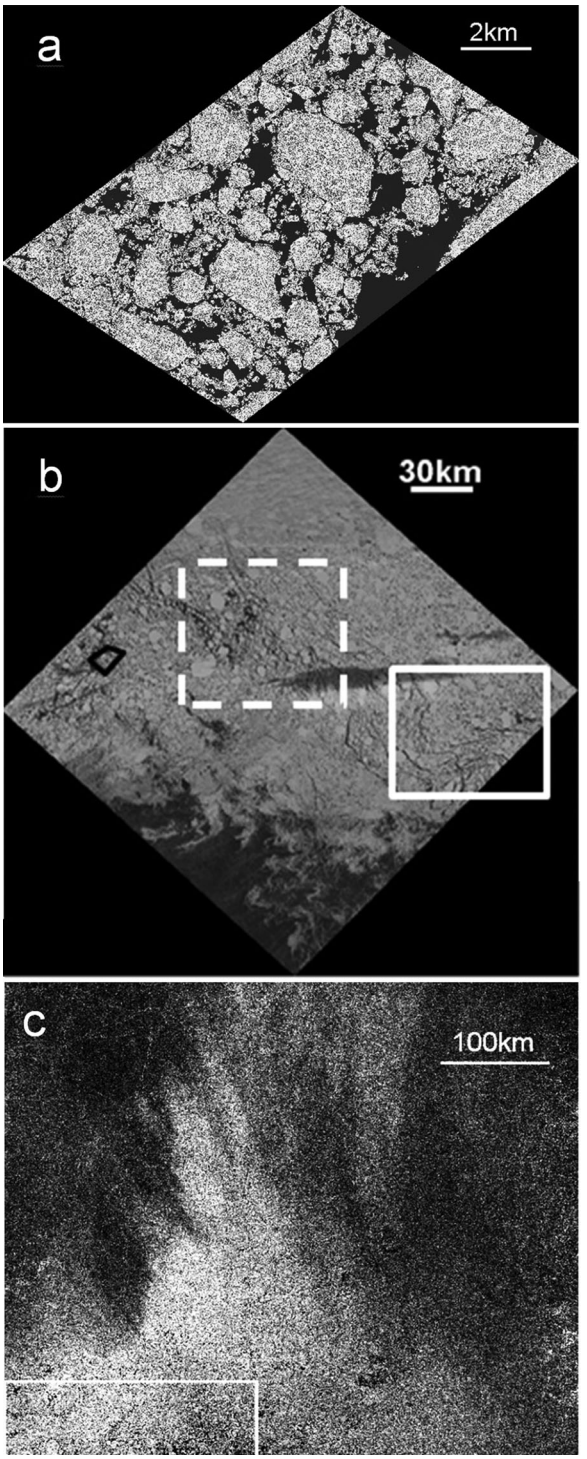

Figure 4. Sample images. (a) MEDEA (M76N0816); (b) Landsat8 (L78N0917) (L1); and (c) RADARSAT-2 (R0802 ©MacDonald, Dettwiler and Associates Ltd., 2014 - All Rights Reserved). The black box in Figure 4b exemplifies the size of Medea image on the Landsat8 scene. The white solid (subscene 1) and dashed (subscene 2) boxes in Figure 4b are used to check the homogeneity of the FSD within the Landsat8 image. The white box in Figure 4c is the portion of the RADASAT-2 used for the FSD analysis. The black frame around all Landsat8 images comes with the images. Its orientation for each image is fixed at x:E-W and y:N-S.

Holt and Martin [2001] reported the August 1992 sea ice cover response to a storm in the Beaufort, Chukchi, and East Siberian Seas using a variety of active and passive microwave satellite data. They examined two locations, one near the ice edge and another in the interior of the ice cover. They found that the storm, identified as an event with peak geostrophic winds of about 18 m/s, fractured the ice cover and shifted the FSD toward smaller floes. The established measure of FSD defined by the slope α in the cumulative floe size distribution $N(d) \sim d^{-\alpha}$ [*Rothrock and Thorndike*, 1984] remained in the 1.8–2.9 range, and did not change by the storm passage.

In *Holt and Martin* [2001] ERS-1 SAR imagery at 25 m resolution was used. The images were averaged to 100 m pixel size to reduce the radar speckle; hence, floes smaller than 100 m could not be observed. Finer resolution studies have been done elsewhere using ship or helicopter observations [e.g., *Lu et al.*, 2008; *Steer et al.*, 2008; *Toyota et al.*, 2006, 2011]. In 1992, there was no direct measurement of wave fields in the Arctic. Global wave models at that time did not cover the Arctic Ocean either. Even though wave conditions were already suggested to cause ice fractures [*Fox and Squire*, 1991], direct linkage between the two was not possible. The *Holt and Martin* [2001] study thus could only compare the ice cover conditions described by floes larger than 100 m with a weather system defined by the wind and atmosphere pressure conditions.

3. Wind and Wave Conditions

To obtain the wind field, we use the data from NOAA NCEP reanalysis. The surface wind from the reanalysis is compared with the daily average of measured SWIFT10 data as shown in Figure 5. The agreement is quite good considering that one was from a model with daily output over a grid resolution of 2.5° and the other a highly sensitive

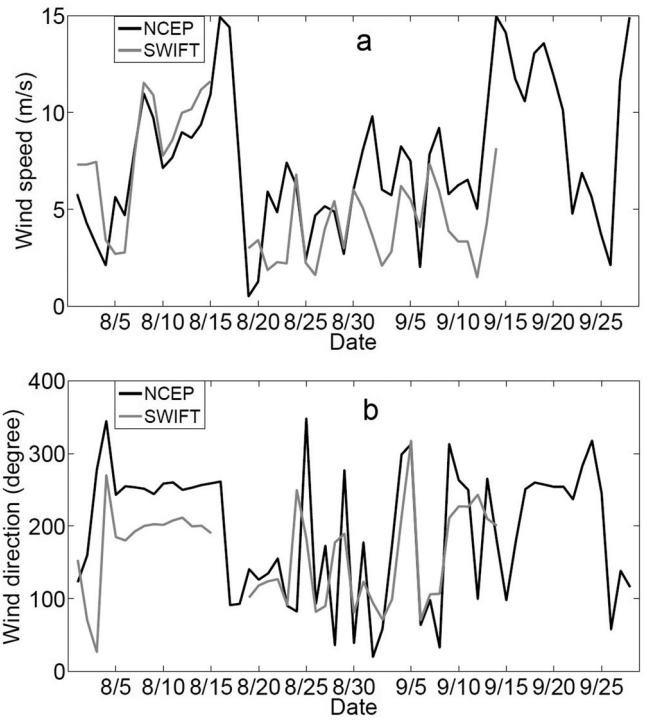

Figure 5. Comparison of sea surface wind from NCEP and from SWIFT10 data. (a) Wind speed and (b) wind direction. The NCEP data were the mean values within a 50 km radius of SWIFT10. The wind direction is defined as 0° = wind from the north. During this period, the correlation coefficient between the NCEP surface wind speed and the SWIFT10 data was 0.6; between geostrophic wind and the measured surface wind was 0.62 with a mean angle between the geostrophic wind and the SWIFT10 at 23.5°.

point-source in situ sensor. We also calculated the geostrophic wind conditions over each of the studied sites (not shown here). All these wind conditions will be used later in this study. Figure 6 shows the time series of the surface wind and the wave condition for August. The image dates are marked by the dark vertical bars. Figure 6a is the NCEP wind speed and direction at the ice edge near the MEDEA and RADARSAT-2 images. In this case, the ice edge is defined as the 15% ice concentration location along the longitude of the MEDEA image locations. Figure 6b is the significant wave height from the WW3 model results. For reference the SWIFT data are superimposed on the model wave data. The two data sets agree quite well when they are collocated as mentioned in section 2. Since the SWIFT data are not at the same location as the model data at the ice edge, their differences indicate the spatial variability of the wave condition along the ice edge. Figure 6c is the WW3 model results of the wave condition at the three MEDEA sites. The model predicts that wave amplitude at the image sites is significantly damped by the ice cover. There is however no measurement yet to verify these predictions. We observe that wind directions on the days of the images were generally off-ice, but wave directions were more on-ice. Figures 7 and 8 are similar plots but for two other groups of images. Figure 7 is for wind and wave conditions near two Landsat8 image locations L1 and L2, and Figure 8 is for the other three Landsat8 image locations L3, L4, and L5. Locations of these images are given in Figure 2c. Again the wind and wave directions were often not aligned. Furthermore, in some cases the wave direction at the chosen ice edge location was quite different from that at the image locations, as shown in Figures 8b and 8c.

4. Image Analysis

We now describe the image analysis for the floe-size distribution and lead identification, orientation, and spacing.

4.1. Floe-Size Distribution

For Landsat8 images, the areas with cloud covers are cropped from the images before analysis. The MEDEA images used are cloud-free but the images have unbalanced brightness. We adopt a brightness balancing method described by *Toyota et al.* [2011]. The whole image is cut into small subregions of 128 by 128 pixels with 50% overlap linearly. For each subregion the 3% highest and lowest pixels are replaced by gray value of 255 and 1, respectively, while the remaining pixels are interpolated linearly between these two values. A median filter is then applied to reduce the speckle noise and smooth the images without influencing the ice edges. Image processing is applied to the image after the above procedures to isolate floes and then determine FSDs. For RADARSAT-2 images, the spatial resolution is on the order of 100 m so that many smaller ice features could not be detected by an automated algorithm. Floes that are identifiable by eye are difficult to separate from the substrate, a term used here that includes interstitial ice consisting of subpixel-sized floes in a mixture of cakes, brash, and water that occurs between larger floes. Manual correction to trace out the floe edges is applied to the extent possible for these images.

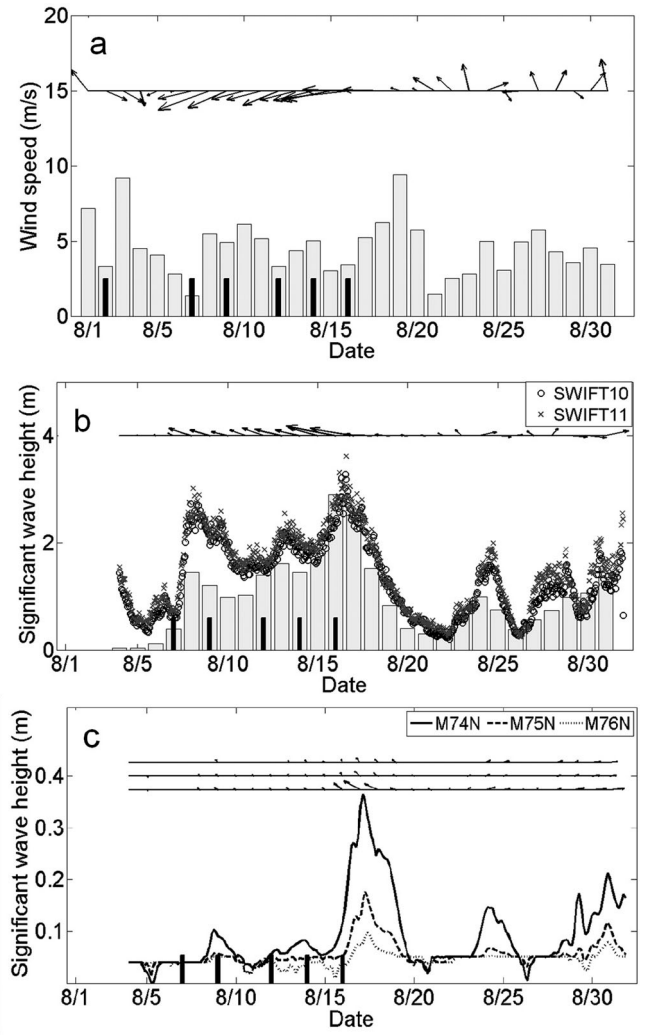

Figure 6. (a) Surface wind speed and direction from NCEP at the ice edge (150°W, 72°N) near the MEDEA and the RADARSAT-2 images. (b) Significant wave height and direction from WW3 at the same ice edge location superimposed with SWIFT wave height. (c) Significant wave height and direction from WW3 at the three MEDEA image locations. The vector plots are arranged from bottom to top to correspond to 74°N, 75°N, and 76°N, respectively. The vertical dark bars in each figure mark the dates of MEDEA images.

Image processing comprises the following sequential steps:

1. *Image enhancement*. The image contrast is further enhanced after the brightness balancing step mentioned earlier. This is done by replacing the highest and lowest 1% of the pixels with the gray scale 255 and 1, respectively, and stretching the remaining pixels by interpolating them between the two levels.
2. *Image segmentation*. An image is segmented based on a technique called local dynamic thresholding [*Haverkamp et al*., 1995], which has been applied to different kinds of sea ice imagery [*Holt and Martin*, 2001; *Lu et al*., 2008]. The image is first subdivided into small regions having 50% overlap with one of their four-neighborhood neighbors. The regions whose histograms are bimodal are selected to calculate the thresholds with the maximum likelihood method. The thresholds are interpolated into all regions [*Chow and Kaneko*, 1972]. Then the pointwise interpolation is applied to make sure each point has its threshold. Most of the floes can be identified after the image is segmented by the local dynamic thresholds.
3. *Floe extraction*. The restricted growing technique [*Soh et al*., 1998] is applied to identify the individual floes and improves the separation of floes that appear to be touching each other. Manual corrections need to be done to define the edge for floes directly touching each other where the segmentation does not work well. In such cases the floe edge line is drawn in order that each floe is principally convex in shape and matches the visual floe pattern.
4. *Substrate identification*. For pixel values that indicate ice is present, but floe edges cannot be clearly identified even visually, we categorize these pixels as substrate as was done in *Holt and Martin* [2001]. Most of this ice is likely smaller or close to the image resolution.

Examples of the output images are shown in Figure 9 together with the input images. Results of the FSD will be presented in section 5.

4.2. Leads Distribution

During the study period, we analyzed a set of Landsat8 images that show a semicontinuous ice cover with clear, quasiperiodic leads. These narrow rectilinear features are openings in the ice that form when an ice cover fails under external forcing, nominally along the thinner portion of the ice cover. Leads only cover a small part of the polar sea ice cover but they have important influence on the heat exchange between the ocean and the atmosphere. Their presence also weakens the ice cover as a whole, enhancing further fracturing and mobility of the ice cover. *Barry et al*. [1989] used Defense Meteorological Satellite Program (DMSP)

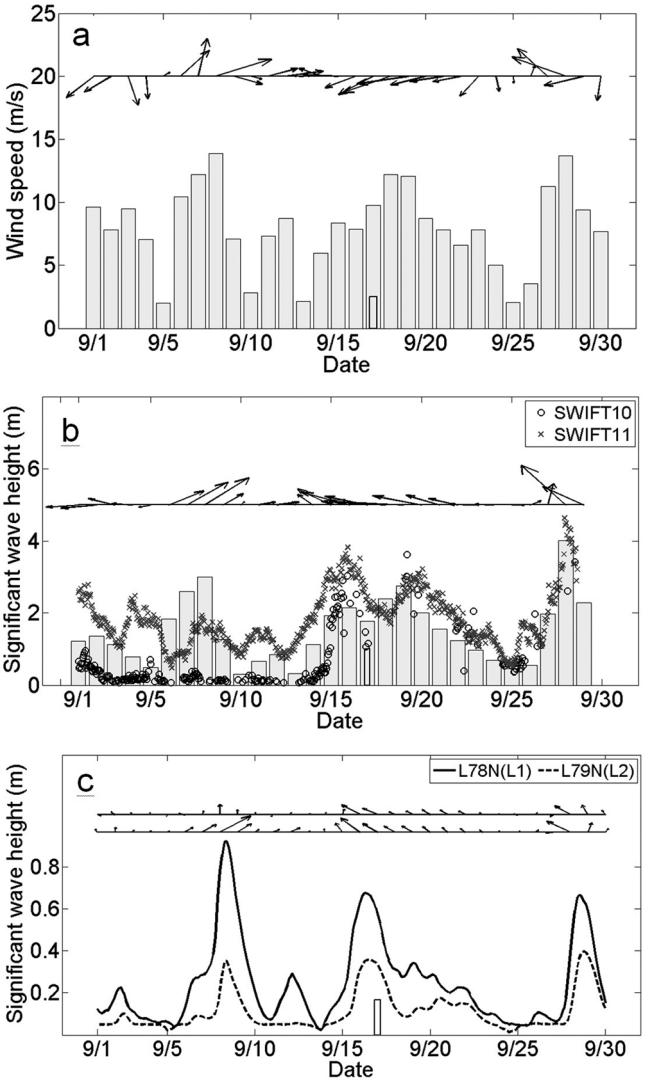

Figure 7. Same as in Figure 6 except near the Landsat8 images L1 and L2 at (165°W, 76°N). The vector plots are arranged from bottom to top to correspond to L1 and L2, respectively. The hollow vertical bar in each figure marks the date of both images (17 September).

imagery to study the lead orientation. In this early work, only very large leads wider than 300 m could be identified. There have been several recent studies of leads frequency, area coverage, and orientation. These studies used AMSR-E passive microwave imagery [*Röhrs and Kaleschke*, 2012; *Bröhan and Kaleschke*, 2014] and CryoSat-2 combined with visible MODIS scenes [*Wernecke and Kaleschke*, 2015]. The spatial resolutions of these studies were at 500 m (CryoSat-2 and MODIS) and 6.25 km (AMSR-E), respectively. Because of these coarse resolutions, again only larger leads could be analyzed.

In this study, we focus on two properties of the leads in the Landsat8 images using much finer resolution data than the above studies: the dominant orientation and spacing between leads, and investigate if these two properties are correlated with the wind and wave forcing. Two example images to be analyzed are shown in Figure 10.

To characterize the lead properties, first the skeleton of these input images of ice cover with distributed leads must be obtained. The skeleton consists of only the centerline pixels of each lead including their branches. The idea of this method is explained in *Banfield* [1992] with the algorithm clearly provided in *Naccache and Shinghal* [1984]. To obtain the leads orientation and spacing the following steps are applied:

1. *Lead identification*. The image is smoothed with a local arithmetic mean filter [*Banfield*, 1992]. The binary image is then created based on the smoothed image with thresholding to separate the leads and the nonleads. The binary image is eroded to obtain the skeleton with the Hilditch method [*Naccache and Shinghal*, 1984]. The starting and ending point of each lead is defined as a pixel with only one neighbor that belongs to the same lead. Leads with a skeleton no more than three pixels are removed.
2. *Leads orientation*. To calculate the mean orientation, the skeletons longer than 1000 m end to end are selected. Leads that are extremely close to each other with their endpoints separated by less than five pixels are connected as one skeleton. Next the *regionprops* function in Matlab is applied to the skeleton of each image, in which the set of distinct leads are defined in the previous step. This function uses an ellipse to fit each lead. The angle between the major axis of the ellipse and the zonal direction defines the orientation of the lead. The mean orientation is defined in two ways. One uses the identical methods as in *Krumbein* [1939], *Curray* [1956], and *Barry et al*. [1989] where the mean direction $\bar{\theta}$ is calculated as $\tan\bar{\theta}=\frac{1}{2}\frac{\sum_{i=1}^{n}\sin 2\theta_i}{\sum_{i=1}^{n}\cos 2\theta_i}$, and the other used the length-weighted mean orientation $\tan\bar{\theta}_w=\frac{1}{2}\frac{\sum_{i=1}^{n}l_i\sin 2\theta_i}{\sum_{i=1}^{n}l_i\cos 2\theta_i}$, where θ_i and l_i is the orientation and the length for each lead, and n is the number of leads.

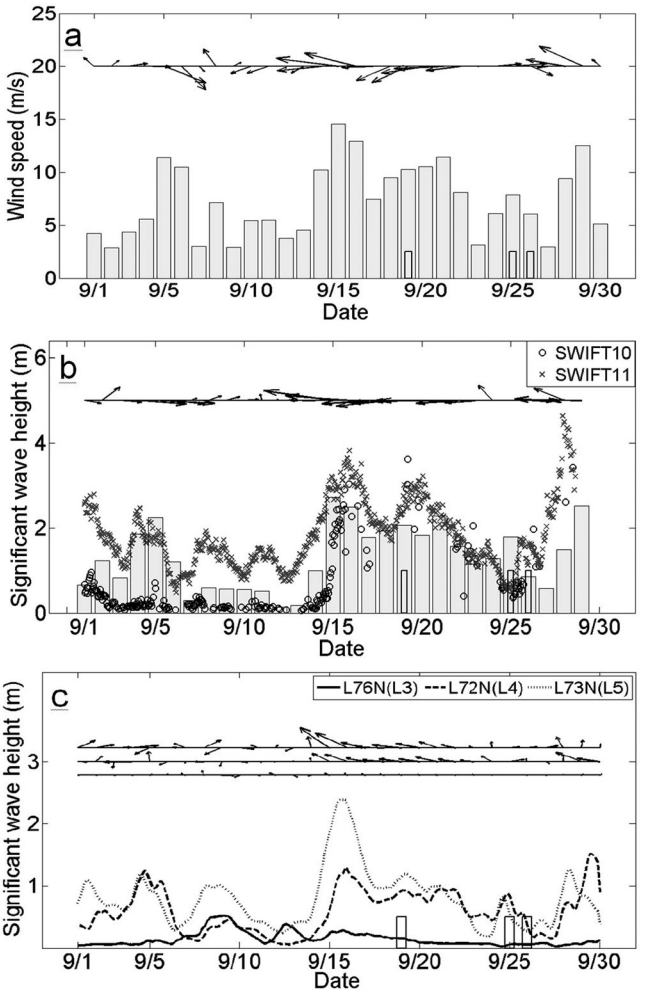

Figure 8. Same as in Figure 6 except near the Landsat8 images L3 and L4 at (135°W, 71°N). The vector plots are arranged from bottom to top to correspond to L3, L4, and L5, respectively. The hollow vertical bars on each figure mark the dates of images.

3. *Leads spacing*. For the spacing between adjacent leads, the center pixel of each lead is located. This center is obtained by a least squares fit to the lead with a straight line first and then the center point of the line is derived. Each lead then looks for the nearest neighbor with a center closest to its own. The normal projection onto the chosen lead of the segment connecting the two centers is defined as the spacing between the lead and the nearest adjacent lead. The arithmetic mean is defined as the mean lead spacing.

For each image the total number of leads before any filtering exceeds 2000. After discarding those less than three pixels in step 1 and applying the connections in step 2, the number of leads analyzed was between 470 and 2100 in each image. Figure 11 provides an example of the above analysis, from the raw image, to binary and to the final skeleton with a collection of leads. For clarity only a subscene from the image is shown.

5. Results of the Image Analysis

5.1. Floe-Size Distribution

Statistical results of the FSD analysis are shown in Figure 12, in which we present the cumulative FSD as defined in *Rothrock and Thorndike* [1984]. The vertical axis is $N(d)$, the number of floes per square kilometer with diameter no less than d. Here we use the mean caliper diameter calculated as $d=\sqrt{A/0.66}$ where A is the floe area [*Rothrock and Thorndike*, 1984]. We separate the Landsat8 results from the rest because they were from different time and location than MEDEA and RADARSAT-2. These FSD curves are fitted with an exponential function $N(d) \sim d^{-\alpha}$. To do so, one needs to be aware of the upper truncation effect due to the limitation of the observation domain size. The finite domain of the images prevents large floes to be included in the FSD. This limitation can artificially steepen the slope at large values of d [*Burroughs and Tebbens*, 2001]. As discussed in *Toyota* [2011], there are two different views concerning the change of slope within an image. One view considered it as a natural result of regime change, where two different slopes govern the smaller and larger sizes of floes [*Steer et al*., 2008]. The other considered it to be strictly the result of upper truncation error [*Lu et al*., 2008; *Stern et al*., 2014]. The results of the traditional single slope and the one modified using the truncation error concept are both listed in Table 1. In order to compare with the earlier analysis from *Holt and Martin* [2001], Table 1 also provides an additional slope of the cumulative FSD for large floes only.

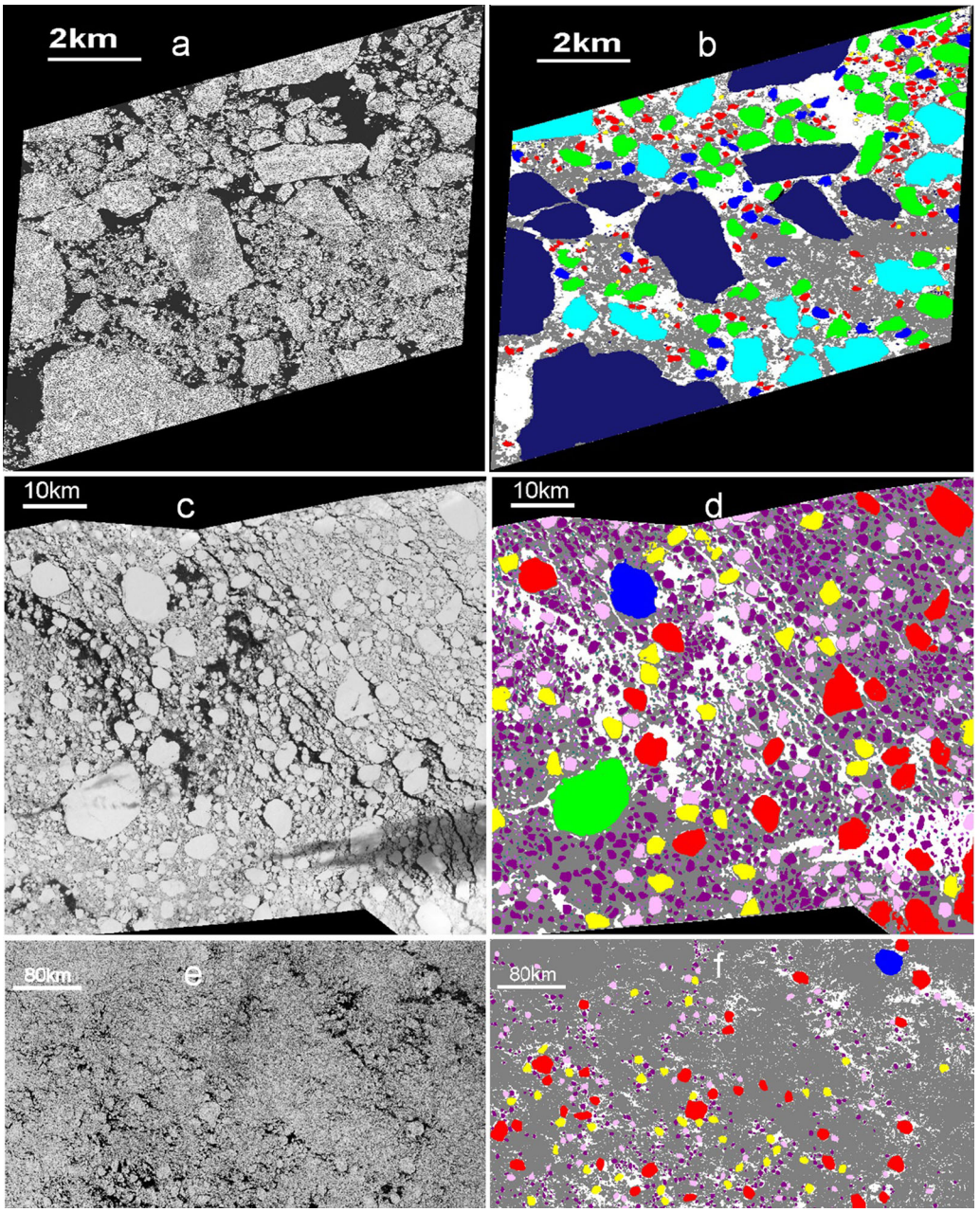

Figure 9. Sample input and output images used for FSD. (a, b) MEDEA, M75N0812, 12 August 2014; (c, d) Landsat8, L78N0917 (L1) subscene 2; (e, f) RADARSAT-2, R0809 (©MacDonald, Dettwiler and Associates Ltd., 2014 - All Rights Reserved).

Because the Landsat8 and RADARSAT-2 images cover a very large area, we are able to use them to study the spatial variation of the ice floe distribution. For example, two regions, solid and dashed (subscene 1 and subscene 2), are marked in the Landsat8 image shown in Figure 4b. We performed the FSD analysis to these two regions separately and found that their cumulative FSD are nearly identical. Hence at least for the region studied and at the time when the image was taken, the FSD is nearly homogenous over the scale of the Landsat8 image. For the RADARSAT-2 images we further partitioned the usable portion of the image into four equal parts and analyzed each part separately. The cumulative FSD for one of such result is shown as the inset in Figure 12a. The other two cases not shown have similar results. The slope of the larger floes remains the same in each of the partitions, but the amount of substrate changes. If we focus only on the behavior of the slopes, the cumulative FSD of the RADARSAT-2 images may be considered uniform over the frame size analyzed.

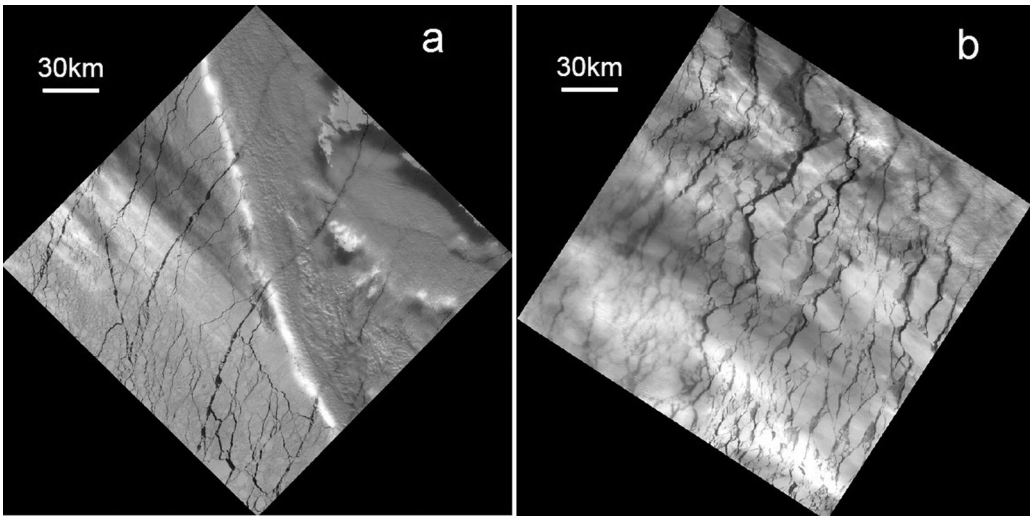

Figure 10. Examples of Landsat8 images used for leads analysis. (a) L78N0920 (L6) and (b) L75N0928 (L15).

In the present FSD analysis, a floe at the edges of the image boundaries may only be partially contained within that image and thus is mislabeled as smaller than its true size. Consequently, the number of the largest floes so obtained is fewer than the reality and that for the smallest floes is artificially increased. Those in between may be changed depending on the true FSD. There is no easy solution to this problem. *Perovich et al*. [2002] proposed using the floe perimeter as a proxy for FSD, and extended that method to estimate the true FSD by correcting the partial inclusion effect [*Perovich and Jones*, 2014]. But their method relies on the assumption that the slope of the cumulative FSD is constant over the entire range of the floe sizes. *Toyota et al*. [2006, 2011] excluded partially enclosed floes from the FSD analysis. Their adjustment artificially increased the percent of open water because the area excluded is pure ice. We choose to acknowledge the error caused by mislabeling the partially enclosed floes, which results in an artificially reduced slope at the largest floe range and an artificially increased slope at the smallest floe range. This error is insignificant for images with a large domain size compared with the largest floe in view. The error increases with reduced domain size.

To get a sense of the distribution in each size bin, we plot the number density FSD in Figure 13. This quantity is defined as $M(d)$, the number of floes per unit area with diameters between $d-\delta_1$ and $d+\delta_2$, where (δ_1, δ_2) is the bin width. Despite being a busy figure, we can clearly see that higher resolution significantly improves our ability to identify smaller floes. For the RADARSAT-2 images with a resolution of 100 m, the number density of floes less than 300 m is not reliable. Likewise, for MEDEA images we should focus on floes greater than 3 m. For Landsat8 the smallest floe size we could detect from the image analysis was 100 m, much larger than the 15 m resolution.

Table 2 summarizes the areas covered by floes, substrate, and open water for all three types of images. The ice concentration measured from the image analysis is compared with the NSIDC data (Table 2), with closer comparisons with Landsat8 than MEDEA results. The correlation coefficient between NSIDC and MEDEA ice concentration is -0.15, with the normalized root-mean-square-difference (NRMSD) equals to 0.23. Between NSIDC and Landsat8 the correlation is 0 and the NRMSD is 0.25. MEDEA images are much smaller than the NSIDC grid, which is about 25 km in linear dimension; hence, we do not expect a close comparison there. The Landsat8 image size is larger than the NSIDC grid size. The seemingly poor correlation between Landsat8 and NSIDC is due primarily to image L5 shown in Figure 14a. Its location is marked in Figure 2c. Half of this image is open water, but our FSD data only include the part covered by ice. The low ice concentration from NSIDC is affected by the open water area in L5. For comparison Figure 14b shows image L3. The lower left part is cloud cover. The location of L3 as shown in Figure 2c is far from the ice edge. If we delete L5 from the comparison with the NSIDC ice concentration, the NRMSD becomes 0.18 with a correlation coefficient of 0.5. This level of agreement is good considering the low number of samples and ambiguity created by a significant amount of substrate in these Landsat8 images. Further discussion of these data combining with the wind and wave conditions given in section 3 will be presented in section 6.

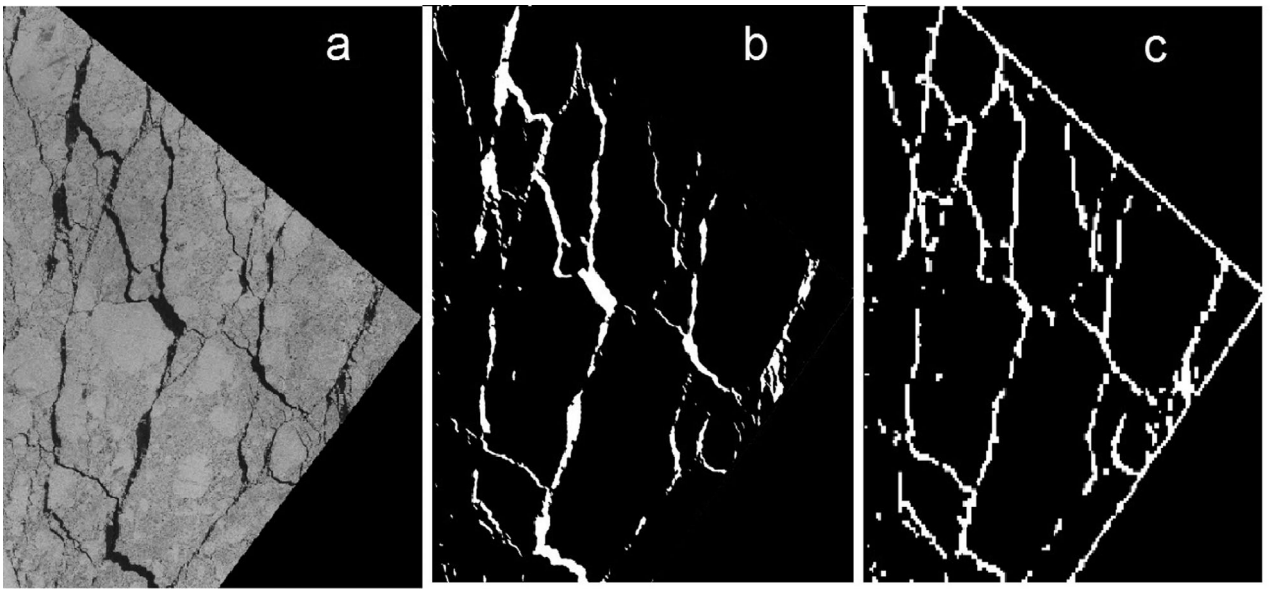

Figure 11. Example of image analysis for leads. (a) Input image; (b) binary image; (c) skeleton image; all from L7/0920.

5.2. Leads Distribution

Instead of the whole Arctic as in previous studies mentioned earlier, here we examine leads in the marginal ice zone and study how they are related to wind and waves. The analysis is carried out for eleven Landsat8 images obtained in September. The ice has gone through both dynamic and thermodynamic processes with much less open water compared with the images obtained in August. Unlike those images from the August period, the air temperature and mean surface temperature (MST) obtained from NCEP were both way below freezing for the September cases (Table 3). Figure 15 presents the distribution of the orientations and spacing between neighboring leads for images L6 and L15 shown in Figure 10. The statistics of both orientation and spacing are scattered. Visual inspection of the imagery shows these leads tend to have different orientations between the long leads and the shorter ones. To obtain a quantitative measure of the orientation and spacing between leads, we separate the leads into three categories according to their length defined by end to end distance: short ($<$1000 m), long ($>$1000 m), and very long ($>$5000 m) leads. We then obtain the mean and standard deviation of the orientation and spacing within each category. These statistical measures are summarized in Table 3, where the mean orientation $\bar{\theta}$ measured from the zonal direction and the length-weighted orientation $\bar{\theta}_w$ are provided. The two mean values $\bar{\theta}, \bar{\theta}_w$ are within 3% of each other for the eleven images. The mean orientations of the three categories are close to each other. The standard deviation for the short leads is consistently the largest of the three categories. The mean lead orientation from our study is similar to

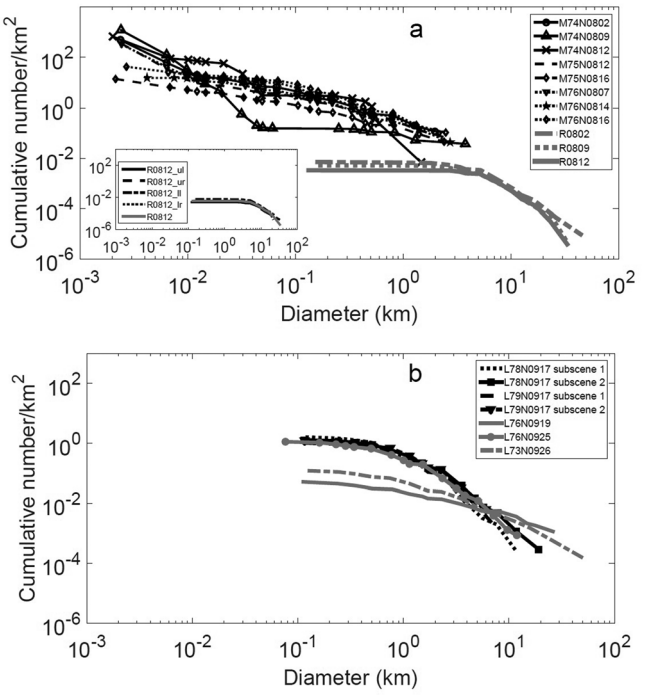

Figure 12. Cumulative floe-size distribution. (a) MEDEA and RADARSAT-2, the inset shows results from partitioned R0812 into four parts: top left (ul), top right (ur), bottom left (dl), and bottom right (dr); (b) Landsat8.

Table 1. The Slope of the Cumulative FSD Curves

Medea	The Slope With Traditional Power Law	The Slope With Truncation Power Law	The Slope With Traditional Power Law (>300 m)	l^a (km)	Ice Thickness (m)
M74N0802	−1.06	−1.78	−1.3	225	1.4
M74N0809	−1.28	−1.9	−0.6	209	1.28
M74N0812	−1.36	−1.4	−2	229	1.22
M75N0812	−1	−1.83	1.25	338	2.0
M75N0816	−0.8	−0.71	−1.07	330	1.83
M76N0807	−1	−1.1	−1.03	443	2.44
M76N0814	−0.9	−1.3	−1.6	434	2.23
M76N0816	−0.9	−2.2	−1.4	440	2.18
Mean	−1.04	−1.53	−0.97		

Landsat8	The Slope With Traditional Power Law	The Slope With Truncation Power Law	The Slope With Traditional Power Law (>1 km)	l (km)	Ice Thickness (m)
L78N0917 (L1 subscene 1)	−1.69	−1.23	−2.80	311	2.3
L78N0917 (L1 subscene 2)	−1.91	−1.14	−2.75	259	2.3
L79N0917 (L2 subscene 1)	−1.64	−0.94	−1.51	399	1.78
L79N0917 (L2 subscene 2)	−1.62	−1.13	−2.44	388	1.78
L76N0919 (L3)	−0.71	−0.38	−0.81	517	1.53
L72N0925 (L4)	−1.67	−1.20	−2.38	126	1.13
L73N0926 (L5)	−1.22	−1.06	−2.52	112	1.48
Mean	−1.49	−1.01	−2.17		

RADARSAT-2	The Slope With Traditional Power Law	The Slope With Truncation Power Law	The Slope for Diameter (>3 km)
R0802	−1.3216	-8.18×10^{-5}	−2.82
R0809	−1.2115	-1.18×10^{-4}	−2.92
R0812	−1.0732	-2.91×10^{-4}	−3.26
Mean	−1.20	-1.6×10^{-4}	−3

[a]l is the distance to the ice edge; the distance to ice edge is skipped for the RADARSAT-2 images due to its very large size.

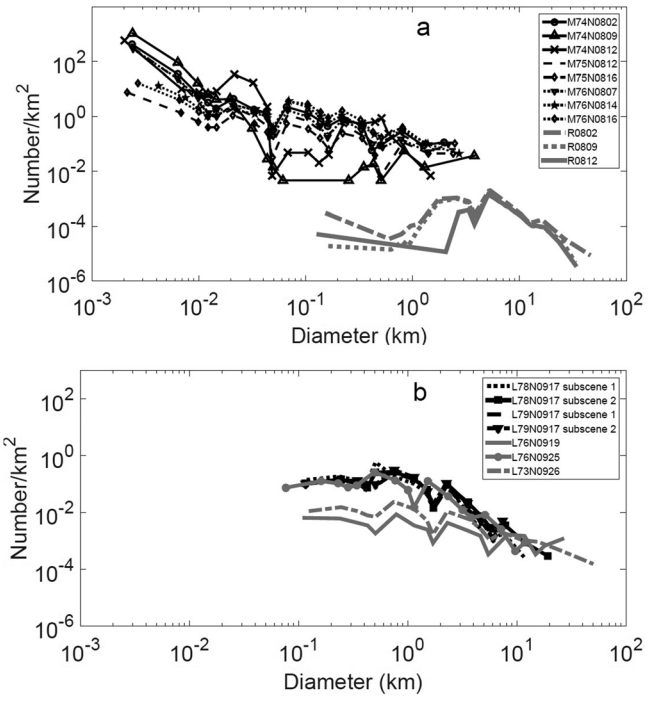

Figure 13. The number density. (a) MEDEA and RADARSAT-2; (b) Landsat8.

Bröhan and Kaleschke [2014], who analyzed the monthly averaged lead orientations in the Beaufort Sea from 2002 to 2011. Their results showed that in the beginning of the winter mean lead orientation was roughly perpendicular to the Alaskan coastline. However, the lead orientation in the Beaufort Sea in September 1988 as reported *Banfield et al.* [1992] had a dominant orientation of 120° counterclockwise from the east. The seasonal and interannual variability of the lead orientation is apparent from these studies.

6. Discussion

6.1. Floe-Size Distribution

The MEDEA FSDs are clustered for those from 75°N and 76°N, but scattered for those from 74°N (Figure 13a). In Figure 16, we separate these number density FSDs shown in Figure 13a into three groups according to their

Table 2. Area Coverage Distribution Among Floes, Substrate, Open Water, and Comparison With *C*:NSIDC Ice Concentration Averaged Over the Entire Frame

Medea	Floe (%)	Substrate (%)	Water (%)	Floe Area (m^2)	C^a (%)	Tair (°C)	MST[b] (°C)
M74N0802	63.3	22.3	14.40	1.28×10^7	57	0.34	−0.11
M74N0809	39.9	21.1	38.99	5.09×10^7	55.4	−0.59	−1.11
M74N0812	37.4	27.3	35.28	3.24×10^7	63.8	−0.75	−1.34
M75N0812	52.5	27	20.53	3.49×10^7	69.4	−0.93	−1.65
M75N0816	31.5	25.9	42.58	2.89×10^7	74.6	−1.40	−2.50
M76N0807	52.5	16.4	31.09	1.24×10^7	73.8	−0.21	−1.28
M76N0814	62.2	11.1	26.72	3.38×10^7	85.7	−0.05	−0.44
M76N0816	58.9	7.8	33.35	5.48×10^7	93.5	−1.50	−2.67
Landsat8	Floe (%)	Substrate (%)	Water	Floe Area (m^2)	*C* (%)	Tair (°C)	MST (°C)
L78N0917 (L1)	41.14	41.6	17.3	2.05×10^9	59.6	−6.97	−6.51
L79N0917 (L2)	41.42	48.6	10	4.34×10^8	81.5	−10.0	−11.1
L76N0919 (L3)	67.12	4.7	28.1	2.67×10^9	71.2	−9.47	−8.29
L72N0925 (L4)	39.21	35.8	25	2.24×10^9	59.1	−3.43	−3.67
L73N0926 (L5)	62.75	27.2	10.1	2.71×10^9	51.4	−5.55	−4.89
RADARSAT-2[c]	Floe (%)	Substrate (%)	Water (%)	Floe Area (m^2)			
R0802	16.42	66.7	16.9	1.95×10^{10}			
R0809	11.62	76.7	11.7	2.44×10^{10}			
R0812	41.66	45.8	12.6	1.07×10^{11}			

[a]The NSIDC ice concentration.
[b]The NCEP mean surface temperature within the respective image frame from both ice-covered and open water regions.
[c]The ice concentration and temperature data are skipped for the RADARSAT-2 images due to its very large size.

latitudes. These MEDEA images were obtained along the same approximate longitude of 150°W, so grouping the results by latitude provides a reference to distance from the ice edge. The ice edge was seen to be retreating west of 150°W but relatively stationary at and to the east of 150°W during the time interval of the MEDEA images (Figure 2b). Recalling that two strong wave events occurred on 7–10 and 15–19 August (Figures (1 and 6)b, and 6c), these FSDs represent the before/after ice cover morphology. From 7–10 August the surface wind at the ice edge was moderate at around 5 m/s (Figures 6a), and the modeled significant wave height ranged from 0.4 to 1.5 m from east-southeast entering the ice edge, at a roughly 70° angle from perpendicular. The second forcing event from 15–19 August showed significant wave heights over 3 m from the east-southeast (Figure 6b) with the surface wind speed at the ice edge from off-ice and moderate. The wave conditions at the same time were mostly from the east-southeast but the surface wind direction was varied. In this group of plots, we observe very little change at the 76°N location (Figure 16a) from 7 to 16 August for sizes less than 10 m. At the 75°N location (Figure 16b) between 12 and 16 August, there is an overall reduction of floe size number. At 74°N (Figure 16c), there is a wide disparity in number density, where the FSD is shown to be largely reducing in number for all sizes larger than 10 m between 2 and 9 August, but increases again between 9 and 12 August.

Table 2 shows that at 76°N over time the amount of water was similar, but increased at 74°N and 75°N. It is not clear what caused this divergent trend over this period, but a more disperse ice field is certainly more susceptible to wave action. At 76°N, during 7–16 August, the air and mean surface temperature (Table 2) shows above sea ice freezing point on 7 and 14 August, then slightly below freezing on 16 August. The calming down of the sea surface after the 7–10 August forcing event together with dropping temperature may explain the reduction of number density in small floes and the increase of the larger ones through aggregation and freezing. At 75°N, the doubling of open water from 12 to 16 August (Table 2) contributes to the general reduction of number density. Changes of the FSD due to other forcing are uncertain for this case. At 74°N from 2 to 12 August, the air temperature and the mean surface temperature (MST) were above freezing (Table 2), consistent with the temperature observation from an ice mass balance buoy in the vicinity (http://imb.erdc.dren.mil/index.htm). The open water area increased between 2 and 9 August then remained stable. Between 2 and 9 August the forcing event was ramping up, then calming down between 9 and 12 August. We thus believe that the decrease in FSD between 2 and 9 August at nearly all diameters less than 10 m at 74°N was likely the result of melting and wave forcing. The forcing apparently was not of sufficient strength or duration to impact the FSD in more northerly image locations. The cause for recovery of the floe number density at 74°N between 9 and 12 August remains uncertain. The MEDEA images are comparatively limited in area, and in the case of the analyzed data set, do not image the same floes, as evidenced by visual

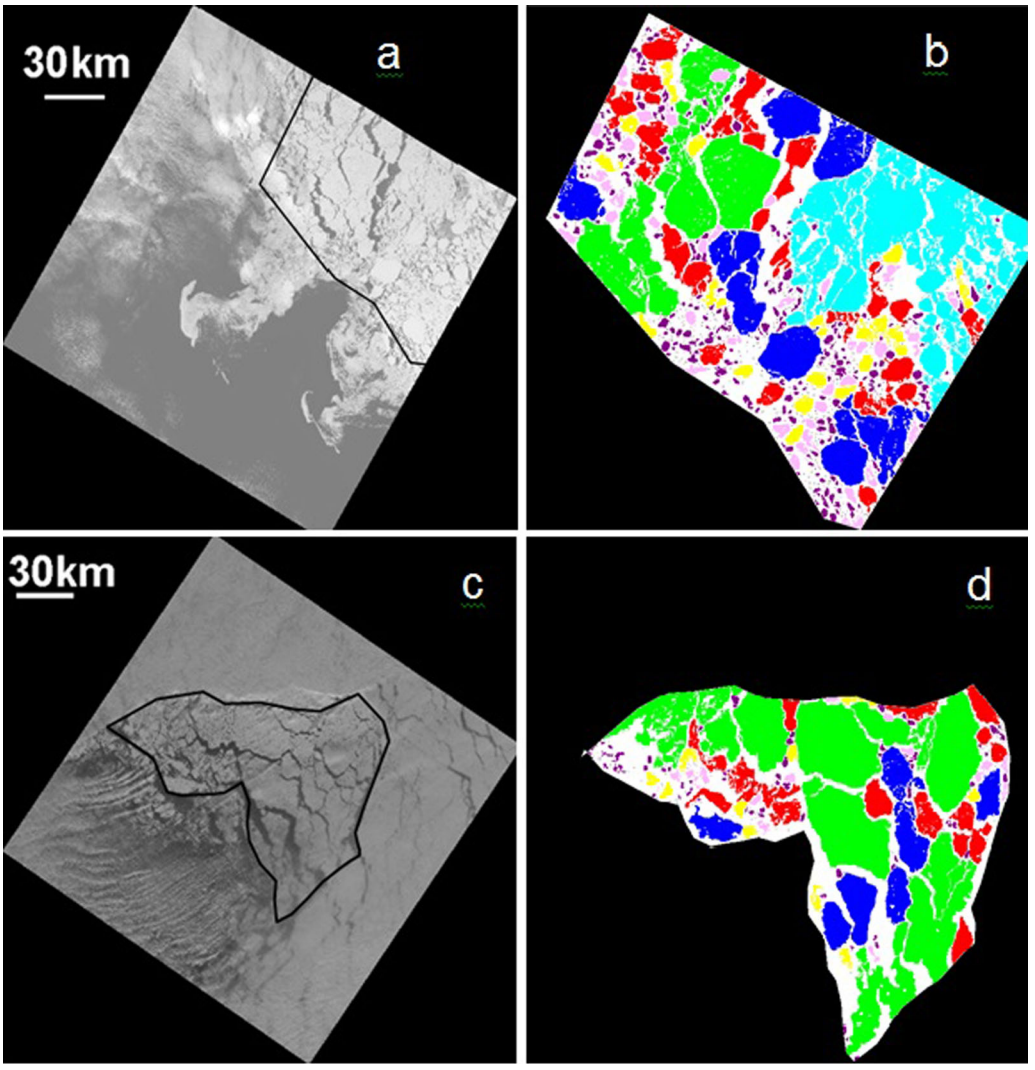

Figure 14. Input and output images of Landsat8 showing transitional development between floes and leads. (a, b) L73N0926 (L5); (c, d) L76N0919 (L3). The analyzed regions are marked in each image.

examination. Clear conclusions as to floe size changes from wave and wind events would benefit greatly from controlled imaging of a floe field by imaging the area around drift buoys over time.

Covering the same dates as the MEDEA imagery located at 74°N, the three RADARSAT-2 data sets shown in Figure 13a indicate no change in the number density for floes larger than 5 km, but continual reduction of floe numbers for those smaller than about 1–3 km. We feel that the RADARSAT-2 FSDs are less conclusive than MEDEA in indicating a change related to wave forcing events.

All Landsat8 images were from September, and as shown in Table 2, during below freezing temperatures. From Figure 12b, the cumulative FSDs were very similar to each other except for L76N0919 (L3) and L73N0926 (L5). The same is also observed in the number density FSDs shown in Figure 13b. On those two days we have substantially fewer floes smaller than 10 km. Closer examination of the input images as shown in Figure 14 indicates that both L76N0919 and L73N0926 were in the early stage of transition between floes and a frozen semicontinuous ice cover, where smaller floes are contained within the now larger, aggregated composite floes. The other images shown in Figure 4b were clearly in the stage where individual floes prevail. Disregarding the L76N0919 and L73N0926 cases, the rest of the Landsat8 cumulative FSD data are consistent, with a slope α between 1.62 and 1.9. L72N0925 (L4) and L73N0926 (L5) are adjacent to each other (Figure 2c). The center of these two images have similar relative distance from the ice edge (Table 1), and experience similar wind and wave conditions (Figure 8) but show quite different FSD and slopes (Figures 12 and 13). Closer examination of these two

Table 3. The Lead Mean Orientation and Standard Deviation[a]

	<1000 m			>1000 m			>5000 m					
	$\bar{\theta}$	$\bar{\theta}_w$	Std_w	$\bar{\theta}$	$\bar{\theta}_w$	Std_w	$\bar{\theta}$	$\bar{\theta}_w$	Std_w	l^b (km)	Tair (°C)	MST (°C)
L6	79.3	78.6	30.8	81.5	79.9	20.4	81.2	80.2	14.8	715	−10.3	−11.3
L7	110.4	113.7	28.9	101.1	97.2	18.2	95.9	93.1	15.5	493	−10.6	−12.3
L8	83.7	83	37.5	86.3	86.4	21.4	88.6	87.5	16.7	384	−5.86	−5.80
L9	101.9	100.5	29.2	88.2	86.3	18.6	85.1	85.8	16.2	756	−7.65	−7.94
L10	83.7	84.2	37.8	87.4	88.7	24	92.7	91.1	17.8	362	−12.2	−13.2
L11	82.6	80.6	39.1	82.2	81.6	24.3	81.6	81.8	17	503	−12.3	−12.8
L12	88.2	89.2	38.7	86.5	84.4	22.1	85.7	83.1	16.5	511	−12.4	−13.1
L13	81.2	79.6	37.5	83.4	83.4	21.3	83.6	83.8	10.5	222	−8.09	−9.35
L14	83.2	88.2	35	86.6	84.4	20.3	84	82.3	14.4	143	−12.2	−13.6
L15	74.8	73.2	33.2	82.6	83.3	18.2	82.5	84.9	13.2	386	−10.7	−11.8
L16	90.8	93.6	39	94.5	93.5	23.6	93.2	93.8	17.9	822	−11.2	−12.5
Mean[c]	87.3	87.7	35.2	87.3	86.3	21.1	86.7	86.1	15.5			

[a]The lead orientation is between 0 and 180. Angles 0 and 180 = zonal direction and 90 = meridional direction. $\bar{\theta}$: arithmetic mean; $\bar{\theta}_w$: length weighted mean; Std_w : length-weighted standard deviation.
[b]Distance to the ice edge.
[c]Mean values of all cases from L6 to L16.

images indicates that L72N0925 (not shown) was dominated by clearly identifiable floes, while L73N0926 was more of a combination of floes and large floe aggregates. The L78N0917 (L1), L79N0917 (L2), and L76N0919 (L3) cases were obtained during higher wind and wave states than L72N0925 and L73N0926 (Figures 7 and 8). A decrease in slope in the cumulative FSD from L79N0917 to L76N0919 is apparent, with L73N0926 having similar slope as L76N0919, despite difference distances from the ice edge, but then L72N0925 slopes return to those of L79N0917. Thus, changes in FSD during and after a passing wind/wave event are not evident. On the other hand, Figure 2c shows interesting ice edge evolution between L79N0917 and L72N0925. Despite the large wind and wave events from 15 to 18 September (Figure 8), the ice edge near L72N0925 remained stationary but it experienced significant advancement near L73N0926. We thus speculate that ice cover morphology and the resulting cumulative FSD might be influenced by the ice cover motion as well.

From Table 2, it is clear that August images were obtained during melt conditions and images in September were obtained during freezing temperatures. All MEDEA and RADARSAT-2 results were from August and all Landsat8 results were from September. Ignoring the truncation issue and focusing on the traditional one-slope results in Table 1 (column 2), small differences of the cumulative FSD slope between seasons are seen, with a slightly steeper slope in September than August. However, if we focus on the larger floes only (column 4), differences between Landsat8 and RADARSAT-2 disappear. It is thus inconclusive if there is an overall seasonal change of the slopes.

For all cases studied, regardless of the season, image resolution or the frame size, the cumulative FSD from each satellite images bends to a shallower slope in the smaller floe sizes range. Bending toward steeper slopes at large floe sizes has been attributed to truncation error as discussed earlier. For Landsat8 and RADARSAT-2 images, since the domains are larger than any of the visible floes enclosed, the falloff of the cumulative FSD curves should be insensitive to "truncation," but could come from some natural upper limit of the floe size, which would also produce a falloff trend. Bending toward a shallower slope toward smaller floes can come from the lack of resolution. This is most obvious from the RADARSAT-2 images. Because of the coarse resolution and large amount of undistinguishable substrate (Table 2), the number of identifiable floes smaller than 2 km was few for RADARSAT-2 images. The cumulative FSD curves thus flatten out for smaller floe sizes (Figure 12a). Furthermore, bending toward a shallower slope at small floe sizes could also result from physical processes. At the smallest scale, in situ observations in the marginal ice zone from several field studies have reported pancake ice [*Lange et al*., 1989; *Doble et al*., 2003], broken ice floes from fracturing [*Wadhams et al*., 1988; *Toyota et al*., 2006, 2011], or brash ice mixed with larger floes [*Wadhams and O'Farrell*, 1985]. Except for brash ice which is too small to identify, both pancake and broken ice floes have some characteristic floe size that presents a lower bound of the FSD. The FSD curve naturally flattens out when approaching these lower bounds defined by mechanical processes. In summer and early fall, lateral melting produces a flattening trend as well [*Perovich and Jones*, 2014].

To further investigate the image resolution issue, we ignore the flattened part of the cumulative FSD curves and focus only on the larger floes in all images. Table 1 (column 4) shows a clear increase of slope with respect to decreasing image resolution, going from MEDEA to Landsat8 followed by RADARSAT-2. The resolution of MEDEA images (1 m) is the closest to the ship-helicopter study reported in *Toyota et al*. [2006, 2011], in which the finest

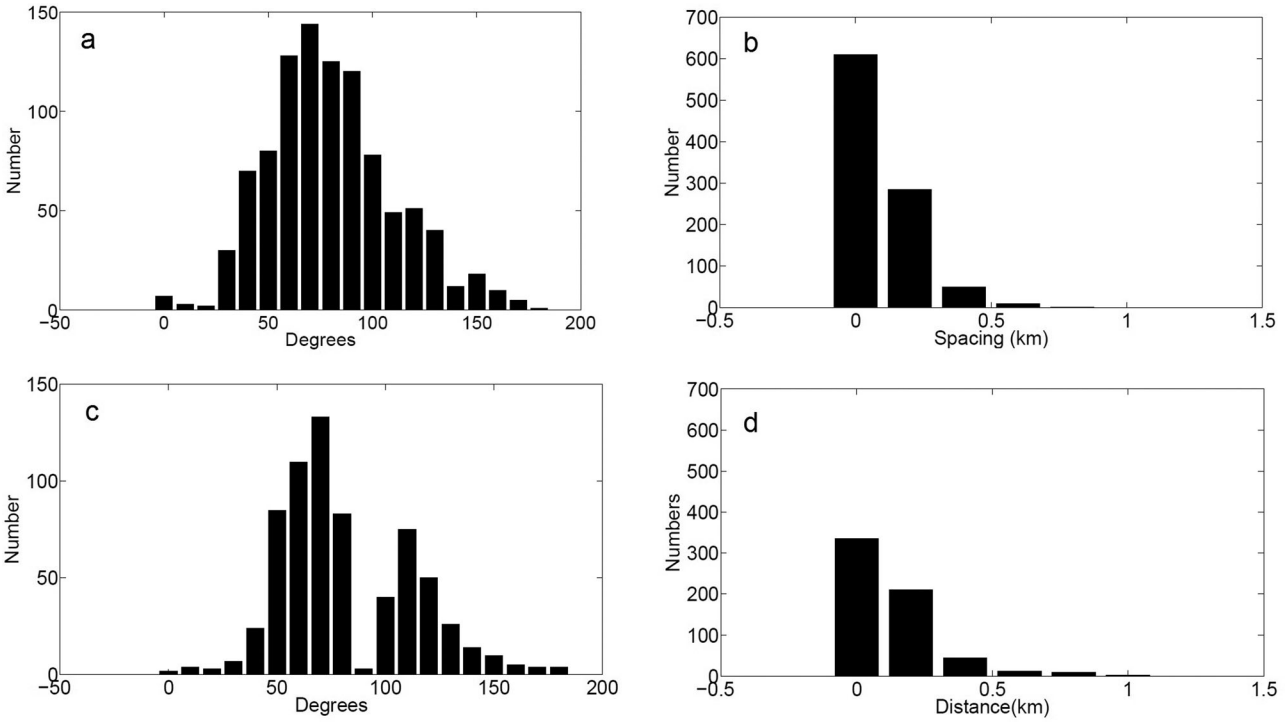

Figure 15. The sample distribution of (a) lead orientation (b) spacing for image L78N0920 (L6) shown in Figure 10a and (c) lead orientation (d) spacing for image L75N0928 (L15) shown in Figure 10b.

resolution was 0.1 m. The image size of their ship-helicopter part of the study was between 400 and 1300 m for the 2006 study and between 200 and 800 m for the 2011 study. Hence, the FSD from the fine resolution part of their study was under the influence of the truncation error. But the FSD behavior from the MEDEA frame size should show an improvement from this effect because the image sizes are now on the order of 10 km. Most of the MEDEA slopes calculated using three different ways as shown in Table 1 were above 1, similar to the results from the fine resolution part of *Toyota et al.* [2006, 2011]. When the two Toyota studies overlaid the slopes from ship, helicopter, and Landsat FSD together, a gradual reduction of the slope of the composite curve similar to what was observed in this study was clear [see *Toyota et al.*, 2006, Figure 3]. Their FSD slopes for the smaller sizes were much shallower than those in the larger sizes. Our MEDEA data show a slightly shallower slope than theirs.

Because of the scale difference, we might not expect that the slope for the small-scale images such as MEDEA and Landsat8 to follow the same FSD distribution as the RADARSAT-2 images studied here or the ERS-1 SAR images used in *Holt and Martin* [2001], and those from MODIS used in *Stern et al.* [2014]. Figure 17 compares the results from RADARSAT-2 and those from ERS-1 SAR in *Holt and Martin* [2001], with both using 100 m resolution images. Both results are from August and occur in similar regions and latitudes. If we consider only the portion of FSD that appears to have quasi-linear slopes before the slopes flatten out, then the two sets of FSD appear very similar. Holt and Martin considered the linear region to be for floes greater than 1 km in diameter while this study shows that region to be greater than 3 km. The high percentage of the substrate from the present cases of RADARSAT-2 images reduced the population of floes across the board, and particularly so for smaller sizes because they are much more difficult to separate from the substrate. The differences then seen in Figure 17 are likely more related to the overall ice characteristics and resulting differences in radar backscatter that may mask the clear identification of smaller floes.

If we may use the MEDEA images to help envision what could happen inside this substrate, we see a large amount of the smaller floes. If we make the bold conjecture that the MEDEA FSD in the same time period and roughly the same location could be used to extend the RADARSAT-2 data, we can see from Figure 12a that there is a much smoother slope change from the larger floe sizes in the RADARSAT-2 to that of the MEDEA data set.

It is worth noting that in *Stern et al.* [2014] another set of cumulative FSD data from TerraSAR-X imagery in the same study area and time of the MODIS images showed the same steep slope in the large floe size range. The Terra SAR-X images used had an 8 m resolution, hence was able to discern much smaller floes. The FSD curve from TerraSAR-X showed a gradual flattening over smaller floes as observed in this study (as well as in *Holt and Martin*

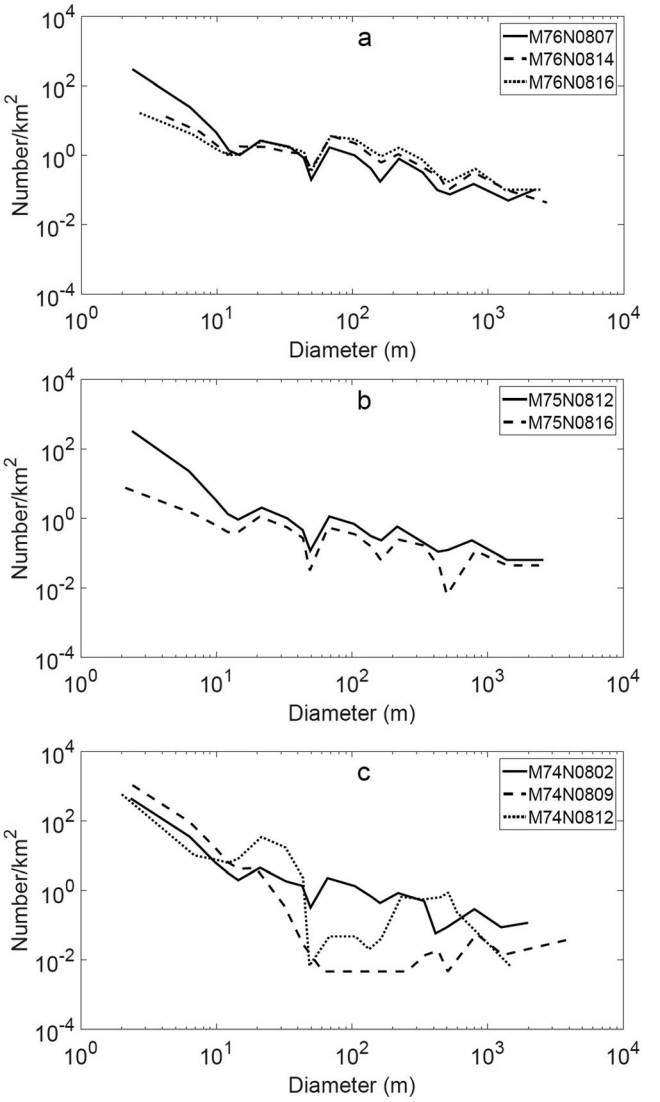

Figure 16. The number density of floe size distribution obtained from the MEDEA images at (a) 76°N, (b) 75°N, and (c) 74°N.

[2001, Figure 11]). We thus conclude from the above mentioned observations that there seems to be a gradual change of the cumulative FSD from large to small floe sizes. For the current data set shown in Table 1, when we focus only on the larger floes in each image, the mean α from MEDEA, Landsat8, and RADARSAT-2 are 0.97, 2.17, and 3, respectively. The latter two are within the same range as in *Holt and Martin* [2001] and *Stern et al.* [2014].

If bending failure is the only mechanism, floe size will ultimately be limited in diameter dependent on its ice thickness [*Mellor*, 1986]. There are no direct observations of ice thickness during this period and location that we are aware of, and because the data are located in the marginal ice zone, possible thickness data derived from CryoSat-2 may not be reliable. To get some understanding of thickness, NCEP-modeled thickness was obtained (Table 1), which shows that at the MEDEA sites the ice thickness was between 1.22 and 2.44 m. For this range of ice thickness, the smallest ice floe that can fracture due to bending is about 20 m [*Mellor*, 1986]. Hence, the increase of very small floes observed could also be due to thermal or other mechanical processes. The average ice thickness of *Holt and Martin* [2001] from the NCEP data was 1.47 m in the Beaufort Sea and 1.57 m in the Chukchi Sea for their study period. These values are similar to the present study. We note that the simulated wave conditions compared to the buoy observations at these two locations during the period of the MEDEA images were quite low, with the significant wave height roughly doubled between 76°N and 75°N, but both below 0.1 m. It is unlikely that such thick ice can be fractured by waves at this low energy. However, the modeled wave conditions have not been verified by any field data, and certainly the model parameters chosen do

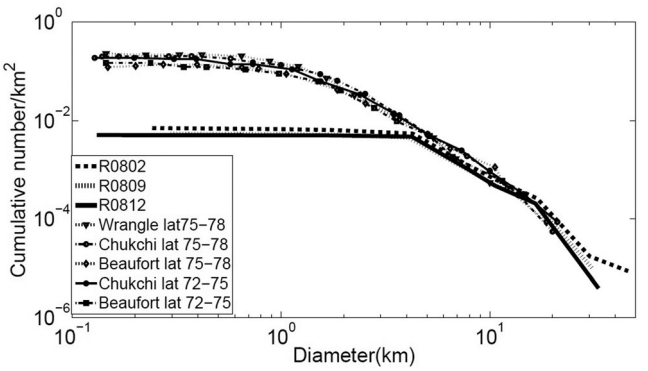

Figure 17. Comparison of RADARSAT-2 and ERS-1 SAR results. The symbol line curves are from *Holt and Martin* [2001] during the August period at similar latitudes of the present data.

have direct influence on the wave height; hence, it is inconclusive to what extent the small floes were the result of fracturing due to wave bending, or other mechanisms related to the wave energy entering the ice cover. As mentioned earlier, during the two August wave events, except 16 August, both air temperature and MST were above freezing for the seawater in the region. We thus speculate melt rates may also play a key role. However, we do not have appropriate observations of how the change in floe size may have resulted from melting rates [*Steele*, 1992], which would require repeating high-resolution imaging of the same floes and region. Finally, we note that floe breakup may result from floe-floe interactions due to ice field deformation, especially in the interior region.

6.2. Lead Orientation and Spacing

To evaluate the correlation of the lead orientation with the wind direction, we adopt the method of *Barry et al*. [1989], where the orientation correlation was calculated as $r_B = n^{-1}\{(\sum_{i=1}^{n}\cos(\delta_i))^2 + (\sum_{i=1}^{n}\sin(\delta_i))^2\}^{1/2}$, where n is the number of samples and δ_i is the angle between the mean lead direction and the geostrophic wind direction. *Barry et al*. [1989] analyzed the lead orientations with the Defense Meteorological Satellite Program (DMSP) images in the Beaufort Sea. The DMSP image resolution was 600 m. Their study spanned from 1980 to 1985 and covered the seasonal periods of January–May and November–December. The study region was 70°N–85°N and 130°W–160°W, including both the interior and marginal zone of the ice cover. They found that the orientations of leads wider than 300 m were broadly correlated with geostrophic wind direction. The mean correlation coefficient between the same day geostrophic wind direction and the leads direction for the fall season was 0.7, with a range of 0.62–0.83.

We used the above definition to calculate the correlation between the directions of geostrophic wind and leads, surface wind and leads, and between waves and leads. All three lead length categories have very similar correlation values (∼0.89) with the geostrophic wind. However, with the NCEP surface wind the correlation coefficients become (0.54, 0.60, and 0.61, respectively). The correlation values with the mean wave direction are (0.76, 0.78, and 0.78, respectively) and slightly better with the peak wave direction (0.81, 0.80, and 0.79, respectively). The correlation with the geostrophic wind is higher than reported in *Barry et al*. [1989], but not too far from their maximum value. We note that our results are from images of very different resolutions from *Barry et al*. [1989]. It is surprising to observe that the lead orientation, regardless of its size, is not better correlated with the surface wind. Realizing that surface wind is very difficult to model, especially for the marginal ice zone, due to the unknown effects of ice cover on the atmosphere boundary layer and the associated drag coefficient, it might be understood why lead correlation with the geostrophic wind could be better than with the surface wind.

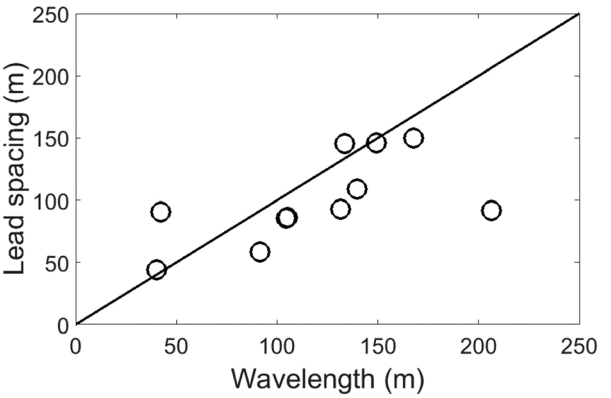

Figure 18. The lead spacing is compared with the wavelength calculated using the peak wave period $T_p = 1/f_p$, where f_p is from the WW3 model results.

Next we compare the lead spacing data with peak wavelength. To do so we only consider the smaller leads because leads longer than 1000 m are spaced too far apart to be impacted by waves. Figure 18 shows the comparison of the mean lead spacing from the short (<1000 m) leads

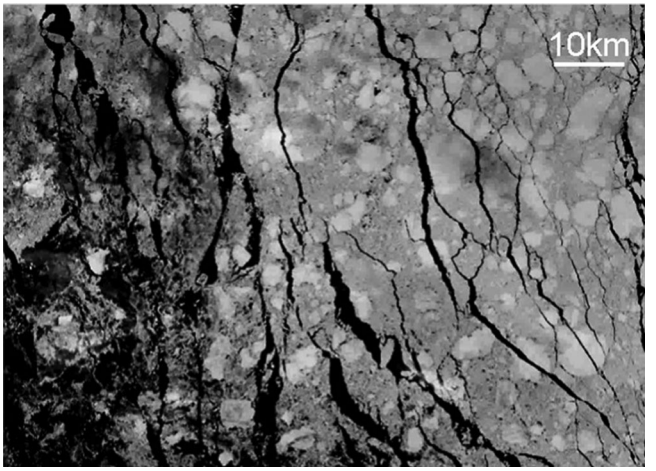

Figure 19. A subscene of Landsat8 image L7 (L780920) showing refrozen floes and leads.

with the wavelength calculated from WW3 at the image locations and times. Except for the outlier with a wavelength over 200 m (L16), there is close agreement. The correlation coefficient between the peak wavelength and the spacing between short leads is 0.6 when considering all eleven samples, and 0.8 if excluding L16. The NRMSD between the two data sets is 0.4 with or without L16. We do not find any agreement of the spacing data with wavelength for larger leads. In *Williams et al.* [2013a] it was assumed that if waves were sufficient to fracture a uniform ice cover through bending, then the maximum floe size would be half the wavelength. Leads are different from floes. They may form from fracturing a continuous ice cover, or from compacting and refreeze existing floe aggregates, such as shown in Figure 19. The latter is particularly plausible in the September MIZ due to rapidly dropping air temperature and solar radiation. High wave action other than pure bending during this time period likely has created the semiperiodic openings observed.

7. Conclusions

To investigate the wind and wave forcing on the ice cover morphology, we analyzed the FSD and lead distribution in the Beaufort and Chukchi Seas in addition to the wind and wave conditions during the summer-fall transition in 2014. Three scales of image resolution are used: 1, 15, and 100 m. Although most of the images are not coincident or collocated, due to the scarcity of available images, and due to the extensive cloud cover in many of the images, we find indication of the wind and wave effect on the ice cover morphology near the ice edge. These findings are summarized below:

1. The FSD from MEDEA images indicates that the wind and wave have different effects on the FSD at different distances to the ice edge, as shown in Figure 16. As expected, the floes near the ice edge are more vulnerable than those in the interior.
2. Bending of the cumulative FSD curve appears to be a universal characteristic among many studies that cover a broad range of resolution and frame size. While artificial bending toward a steeper slope could be introduced by the truncation of a finite image size, far from this upper limit the FSD should be free from this error. The shallowing of the slope toward the smaller sizes may result from a minimum floe size that is mechanically achievable, in addition lack of resolution to detect small floes. During melt season, lateral melting further reduces the floe size. FSD evolution under both mechanical and thermodynamic forcing has only recently been studied by *Perovich and Jones* [2014]. Their study was over a seasonal scale, rather than focusing on storm effects. It is however interesting to note that their results show melting flattens the cumulative FSD curve for floes smaller than 100 m.
3. Our data also suggest a transitional stage between loose floes to leads forming in a semicontinuous, aggregated ice cover. In this transition, the slope of the cumulative FSD increases with a shallower slope in the more lead-like stage and a steeper slope in the more floe-like stage.
4. Lead orientation correlates with wind and the wave direction. The correlation coefficient with the geostrophic wind is better than what was found in a previous study [*Barry et al.*, 1989] which used much coarser spatial resolution data but with larger temporal and areal coverage.
5. There is a correlation between the lead spacing of short leads and the peak wavelength for all but one of the eleven images analyzed. This correlation does not seem to depend on the distance to the ice edge for the range of distances shown in Table 3. For larger leads the spacing is more likely produced by wind and internal stress than the wave action. It would be an interesting future study to separate the large and small leads in order to determine what the respective mechanisms are responsible for their formation.

The present study does not quantify how waves and wind change the ice cover. The data set is too sparse. Intensive measurements before/during/after a storm are needed to confidently determine these fine-scale processes. Coincident and collocated images of the ice cover and in situ wave and wind data must be obtained in order to perform such a quantitative study. With the ongoing integrated field programs mentioned in section 1, we expect such quantitative studies using comprehensive data collections will be possible very soon.

Appendix A: Details of all Imageries Used

In this appendix all satellite images used in this paper are listed with its name, date, center location, coverage, and resolution.

Table A1. MEDEA Images for Floe-Size Distribution

File Name	Date	Center Location	Resolution (m)	Analyzed Area (km^2)
sizr74n20140802 (M74N0802)	2 Aug	149.86°W, 74.05°N	1	20.2
sizr74n20140809 (M74N0809)	9 Aug	149.98°W, 73.89°N		128
sizr74n20140812 (M74N0812)	12 Aug	149.79°W, 74.07°N		86.6
sizr75n20140809 (M75N0809)	12 Aug	149.8°W, 75.7°N	1	66.5
sizr75n20140812 (M75N0812)	16 Aug	150.36°W, 74.98°N		91.6
sizr76n 20140807 (M76N0807)	7 Aug	149.98°W, 76.02°N	1	23.6
sizr76n 20140814 (M76N0814)	14 Aug	150.16°W, 75.94°N		54.3
sizr76n 20140816 (M76N0816)	16 Aug	150.4°W, 75.95°N		93.1

Table A2. The Landsat Images for Floe-Size Distribution

File Name[a]	Date	Center Location	Resolution (m)	Frame Size[b] (km^2)	Analyzed Area (km^2)
LC80930042014260LGN00 (L1)	17 Sep	78.13°N, 158.04°W	15	275.1 × 275.1	4.98×10^3 [c] 3.52×10^3[d]
LC81020032014260LGN00 (L2)	17 Sep	79.12°N, 166.56°W	15	273.9 × 273.3	1.06×10^3 [c] 9.17×10^2[d]
LC80750062014262LGN00 (L3)	19 Sep	75.90°N, 138.63°W	15	270 × 270.9	3.98×10^3
LC80690092014268LGN00 (L4)	25 Sep	72.24°N, 137.95°W	15	258.9 × 260.5	5.71×10^3
LC80760082014269LGN00 (L5)	26 Sep	73.47°N, 146.31°W	15	265.5 × 266.7	4.32×10^3

[a]LC8 = Landsat8, 093 = path, 004 = row, 2014 = year, 260 = Julian day.
[b]The actual image size is 185 × 185 km^2; the frame includes the black region that came with the image.
[c]The subscene 1 size.
[d]The subscene 2 size.

Table A3. The Dates and Locations of the RADARSAT-2 Images

File Name[a]	Date	Center Location[b]	Resolution (m)	Analyzed Image Area[c] (km^2)
20140802225650 (R0802)	2 Aug	144.64°W, 76.35°N	100	232 × 130
20140809225228 (R0809)	9 Aug	143.68°W, 76.44°N	100	283 × 188
20140812230323 (R0812)	12 Aug	140.53°W, 76.31°N	100	346 × 191

[a]File name 2014 = year, 08 = month, 02 = day, 22 = hour, 56 = minute, 50 = second.
[b]The center locations and frame sizes of the subscenes analyzed.
[c]The full images have a nominal size of 500 km × 500 km and the center locations of the full images are around 138.85°W, 77.9°N.

Table A4. The Dates and Locations of the Images Used for the Lead Analysis

File Name	Date	Center Location	Resolution (m)
LC80820042014263LGN00 (L6)	20 Sep	78.12°N, 141.04°W	15
LC80820052014263LGN00 (L7)	20 Sep	77.05°N, 145.57°W	15
LC80730072014264LGN00 (L8)	21 Sep	74.71°N, 138.83°W	15
LC80870032014266LGN00 (L9)	23 Sep	79.12°N, 143.37°W	15
LC80850052014268LGN00 (L10)	25 Sep	77.05°N, 150.21°W	15
LC80850042014268LGN00 (L11)	25 Sep	78.13°N, 145.67°W	15
LC80760062014269LGN00 (L12)	26 Sep	75.90°N, 140.17°W	15
LC80830062014270LGN00 (L13)	27 Sep	75.90°N, 150.99°W	15
LC80830052014270LGN00 (L14)	27 Sep	77.05°N, 147.13°W	15
LC80740072014271LGN00 (L15)	28 Sep	74.71°N, 140.39°W	15
LC80740062014271LGN00 (L16)	28 Sep	75.90°N, 137.09°W	15

Acknowledgments

The first author is a visiting doctoral student at Clarkson University. The financial support of China Scholarship Council (201306330026), National Natural Science Foundation of China (41521091, U1406401) and the hospitality of Clarkson University are appreciated. This work was supported in part by the Office of Naval Research, including grants N00014-13-1-0294, N0001413WX20825, and N00014-12-1-0113. This work was also performed at the Jet Propulsion Laboratory, California Institute of Technology under contract with the National Aeronautics and Space Administration, with support from the Office of Naval Research (grant N0001415IP00081). We thank William Olsen of Clarkson University for his generous guidance in using ArcGIS for part of the image analysis, and the insightful suggestions from the anonymous reviewers. The data used in this study are all provided in the references cited. They are also listed below: air temperature (http://www.esrl.noaa.gov/psd/cgi-bin/DataAccess.pl?DB_dataset=NCEP+Reanalysis+Daily+Averages+Surface+Level&DB_variable-Air+temperature&DB_statistic=Mean&DB_tid=48141&DB_did=33&DB_vid=668); ice mass balance buoy data (http://imb.erdc.dren.mil/index.htm); ice thickness data (http://rda.ucar.edu/datasets/ds093.0/#!access); Landsat8 data (http://LandSAT.usgs.gov/Landsat8.php); MEDEA data (http://gfl.usgs.gov/); RADARSAT-2 data (http://www.apl.washington.edu/project/project.php?id=arctic_sea_state); sea surface mean surface temperature, MST (http://www.esrl.noaa.gov/psd/cgi-bin/DataAccess.pl?DB_dataset=NCEP+Reanalysis+Daily+Averages+Surface+Flux&DB_variable=Temperature&DB_statistic=Mean&DB_tid=48141&DB_did=34&DB_vid=1282); SWIFT10 camera record (http://faculty.washington.edu/jmt3rd/SWIFTdata/ArcticOcean/SWIFT10_Sep1_Sep15_Timelapse.mp4); wave data (http://apl.uw.edu/swift); wind data source (http://www.esrl.noaa.gov/psd/data/gridded/data.ncep.reanalysis.surface.html); RADARSAT-2 images were collected by the Center for Southeastern Tropical Advanced Remote Sensing (CSTARS) in support of the Marginal Ice Zone program and made available for use within the related Sea State program.

References

Banfield, J. (1992), Skeletal modeling of ice leads, *IEEE Trans. Geosci. Remote Sens.*, *30*, 918–923, doi:10.1109/36.175326.

Barry, R. G., M. W. Miles, R. C. Cianflone, G. Scharfen, and R. C. Schnell (1989), Characteristics of Arctic sea ice from remote-sensing data and their relationship to atmospheric processes, *Ann. Glaciol.*, *12*, 9–15.

Bröhan, D., and L. Kaleschke (2014), A nine-year climatology of Arctic sea ice lead orientation and frequency from AMSR-E, *Remote Sens.*, *6*, 1451–1475, doi:10.3390/rs6021451.

Burroughs, S. M., and S. F. Tebbens (2001), Upper-truncated power laws in natural systems, *Pure Appl. Geophys.*, *158*, 741–757.

Chow, C. K., and T. Kaneko (1972), Automatic boundary detection of the left ventricle from cineangiograms, *Comput. Biomed. Res.*, *5*, 388–410, doi:10.1016/0010-4809(72)90070-5.

Cunningham, G. F., R. Kwok, and J. Banfield (1994), Ice lead orientation characteristics in the winter Beaufort Sea, in *IGARSS'94. Surface and Atmospheric Remote Sensing: Technologies, Data Analysis and Interpretation*, International, vol. 3, pp. 1747–1749, IEEE, Pasadena, Calif., doi:10.1109/IGARSS.1994.399553.

Curray, J. R. (1956), The analysis of two-dimensional orientation data, *J. Geol.*, *64*, 117–131.

Doble, M. J., M. D. Coon, and P. Wadhams (2003), Pancake ice formation in the Weddell Sea, *J. Geophys. Res.*, *108*(C7), 3209, doi:10.1029/2002JC001373.

Fetterer, F., and N. Untersteiner (1998), Observations of melt ponds on Arctic sea ice, *J. Geophys. Res.*, *103*(C11), 24,821–24,835, doi:10.1029/98JC02034.

Fox, C., and V. A. Squire (1991), Strain in shore fast ice due to incoming ocean waves and swell, *J. Geophys. Res.*, *96*(C3), 4531–4547, doi:10.1029/90JC02270.

Haverkamp, D., L.-K. Soh, and C. Tsatsoulis (1995), A comprehensive, automated approach to determining sea ice thickness from SAR data, *IEEE Trans. Geosci and Remote Sensing*, *33*(1), 46–57, doi:10.1109/36.368223.

Herbers, T. H. C., P. F. Jessen, T. T. Janssen, D. B. Colbert, and J. H. MacMahan (2012), Observing ocean surface waves with GPS-tracked buoys, *J. Atmos. Oceanic Technol.*, *29*, 944–959, doi:10.1175/JTECH-D-11-00128.1.

Holt, B., and S. Martin (2001), The effect of a storm on the 1992 summer sea ice cover of the Beaufort, Chukchi, and East Siberian Seas, *J. Geophys. Res.*, *106*(C1), 1017–1032, doi:10.1029/1999JC000110.

Kohout, A. L., M. J. M. Williams, S. Dean, and M. H. Meylan (2014), Storm-induced sea ice breakup and the implications for ice extent, *Nature*, *509*, 604–607, doi:10.1038/nature13262.

Krumbein, W. C. (1939), Preferred orientation of pebbles in sedimentary deposits, *J. Geol.*, *47*(7), 673–706.

Kwok, R. (2014), Declassified high-resolution visible imagery for Arctic sea ice investigations: An overview, *Remote Sens. Environ.*, *142*, 44–56, doi:10.1016/j.rse.2013.11.015.

Kwok, R., G. F. Cunningham, M. Wensnahan, I. Rigor, H. J. Zwally, and D. Yi (2009), Thinning and volume loss of the Arctic Ocean sea ice cover: 2003-2008, *J. Geophys. Res.*, *114*, C07005, doi:10.1029/2009JC005312.

Lange, M. A., S. F. Ackley, P. Wadhams, G. S. Dieckmann, and H. Eicken (1989), Development of sea ice in the Weddell Sea, *Ann. Glaciol.*, *12*, 92–96.

Li, J., A. L. Kohout, and H. H. Shen (2015), Comparison of wave propagation through ice covers in calm and storm conditions, *Geophys. Res. Lett.*, *42*, 5935–5941, doi:10.1002/2015GL064715.

Liu, A. K., and E. Mollo-Christensen (1988), Wave propagation in a solid ice pack, *J. Phys. Oceanogr.*, *18*(11), 1702–1712, doi:10.1175/1520-0485(1988)018.

Lu, P., Z. J. Li, Z. H. Zhang, and X. L. Dong (2008), Aerial observations of floe size distribution in the marginal ice zone of summer Prydz Bay, *J. Geophys. Res.*, *113*, C02011, doi:10.1029/2006JC003965.

Lubin, D., and R. Massom (2006), *Polar Remote Sensing: Atmosphere and Oceans*, vol. 1, 756 pp., Springer, Berlin.

Maslanik, J., and J. Stroeve (1999), Near-Real-Time DMSP SSMIS Daily Polar Gridded Brightness Temperatures, http://dx.doi.org/10.5067/AKQDND71ZDLF, Natl. Snow and Ice Data Cent. (NSIDC) DAAC, Boulder, Colo.

Maykut, G. A. (1986), The surface heat ad mass balance, in *The Geophysics of Sea Ice*, edited by N. Untersteiner, pp. 395–464, Plenum, N. Y.

Mellor, M. (1986), The mechanical behavior of sea ice, in *Geophysics of Sea Ice*, edited by N. Untersteiner, pp. 165–281, Springer, N. Y.

Naccache, J. J., and R. Shinghal (1984), An investigation into the skeletonization approach of Hilditch, *Pattern Recognit.*, *17*(3), 279–284.

Overland, J. E., and M. Wang (2013), When will the summer Arctic be nearly sea ice free, *Geophys. Res. Lett.*, *40*, 2097–2101, doi:10.1002/grl.50316.

Overland, J. E., J. A. Francis, E. Hanna, and M. Wang (2012), The recent shift in early summer Arctic atmospheric circulation, *Geophys. Res. Lett.*, *39*, L19804, doi:10.1029/2012GL053268.

Parkinson, C. L., and J. C. Comiso (2013), On the 2012 record low Arctic sea ice cover: Combined impact of preconditioning and an August storm, *Geophys. Res. Lett.*, *40*, 1356–1361, doi:10.1002/grl.50349.

Perovich, D. K., and K. F. Jones (2014), The seasonal evolution of sea ice floe size distribution, *J. Geophys. Res. Oceans*, *119*, 8767–8777, doi:10.1002/2014JC010136.

Perovich, D. K., W. B. Tucker III, and K. A. Ligett (2002), Aerial observations of the evolution of ice surface conditions during summer, *J. Geophys. Res.*, *107*(C10), 8048, doi:10.1029/2000JC000449.

Richter-Menge, J. A., S. L. McNutt, J. E. Overland, and R. Kwok (2002), Relating arctic pack ice stress and deformation under winter conditions, *J. Geophys. Res.*, *107*(C10), 8040, doi:10.1029/2000JC000477.

Rogers, W. E., and S. Zieger (2014), New wave-ice interaction physics in WAVEWATCH III®, paper presented at 22nd IAHR International Symposium on Ice, International Association for Hydro-Environment Engineering and Research (IAHR), Singapore.

Röhrs, J., and L. Kaleschke (2012), An algorithm to detect sea ice leads by using AMSR-E passive microwave imagery, *Cryosphere*, *6*, 343–352, doi:10.5194/tc-6-343-2012.

Rothrock, D. A., and A. S. Thorndike (1984), Measuring the sea ice floe size distribution, *J. Geophys. Res.*, *89*(C4), 6477–6486, doi:10.1029/JC089iC04p06477.

Roy, D. P., et al. (2014), Landsat-8: Science and product vision for terrestrial global change research, *Remote Sens. Environ.*, *145*, 154–172, doi:10.1016/j.rse.2014.02.001.

Simmonds, I., and K. Keay (2009), Extraordinary September sea ice reductions and their relationships with storm behavior over 1979–2008, *Geophys. Res. Lett.*, *36*, L19715, doi:10.1029/2009GL039810.

Simmonds, I., and I. Rudeva (2012), The great Arctic cyclone of August 2012, *Geophys. Res. Lett.*, *39*, L23709, doi:10.1029/2012GL054259.

Soh, L.-K., B. Holt, and C. Tsatsoulis (1998), Identifying ice floes and computing ice floe distributions in SAR images, in *Analysis of SAR Data of the Polar Regions*, edited by C. Tsatsoulis and R. Kwok, pp. 9–34, Springer, N. Y.

Squire, V. A. (1984), A theoretical, laboratory, and field study of ice-coupled waves, *J. Geophys. Res.*, *89*(C5), 8069–8079, doi:10.1029/JC089iC05p08069.
Squire, V. A. (2007), Of ocean waves and sea-ice revisited, *Cold Reg. Sci. Technol.*, *49*(2), 110–133, doi:10.1016/j.coldregions.2007.04.007.
Steele, M. (1992), See ice melting and floe geometry in a simple ice-ocean model, *J. Geophys. Res.*, *97*(C11), 17,729–17,738, doi:10.1029/92JC01755.
Steele, M., W. Ermold, and J. Zhang (2008), Arctic Ocean surface warming trends over the past 100 years, *Geophys. Res. Lett.*, *35*, L02614, doi:10.1029/2007GL031651.
Steer, A., A. P. Worby, and P. Heil (2008), Observed changes in sea-ice floe size distribution during early summer in the western Weddell Sea, *Deep Sea Res., Part II*, *55*, 933–942, doi:10.1016/j.dsr2.2007.12.016.
Stern, H., A. Schweiger, M. Stark, J. Zhang, P. Hwang, T. Kraemer, and M. Steele (2014), The floe size distribution in the marginal ice zone of the Beaufort and Chukchi Seas, Abstract C11A-0349 presented at 2014 Fall Meeting, AGU, San Francisco, Calif., 15–19 Dec.
Stroeve, J. C., V. Kattsov, A. Barrett, M. Serreze, T. Pavlova, M. Holland, and W. Meier (2012), Trends in Arctic sea ice extent from CMIPS, CMIP3 and observations, *Geophys. Res. Lett.*, *39*, L16502, doi:10.1029/2012GL052676.
Thomson, J. (2012), Wave breaking dissipation observed with "SWIFT" drifters, *J. Atmos. Oceanic Technol.*, *29*, 1866–1882, doi:10.1175/JTECH-D-12-00018.1.
Thomson, J., and W. E. Rogers (2014), Swell and sea in the emerging Arctic Ocean, *Geophys. Res. Lett.*, *41*, 3136–3140, doi:10.1002/2014GL059983.
Tolman, H. L. (2003), Treatment of unresolved islands and ice in wind wave models, *Ocean Modell.*, *5*(3), 219–231.
Toyota, T., S. Takatsuji, and M. Nakayama (2006), Characteristics of sea ice floe size distribution in the seasonal ice zone, *Geophys. Res. Lett.*, *33*, L02616, doi:10.1029/2005GL024556.
Toyota, T., C. Haas, and T. Tamura (2011), Size distribution and shape properties of relatively small sea-ice floes in the Antarctic marginal ice zone in late winter, *Deep Sea Res., Part II*, *58*, 1182–1193, doi:10.1016/j.dsr2.2010.10.034.
Wadhams, P. (2000), *Ice in the Ocean*, 351 pp., Gordon and Breach, Amsterdam.
Wadhams, P., and S. P. O'Farrell (1985), The motion of ice edge radar transponders during MIZEX-West, in *MIZEX Bulletin VI:MIZEX-West*, *Spec. Rep. 85-6:50-60*, U.S. Army Cold Reg. Res. and Eng. Lab., Hanover, N. H. [Available at http://acwc.sdp.sirsi.net/client/en_US/search/asset/1010926;jsessionid=BA556F4F255DEE40E07AD5E84E1F7DD4.enterprise-15000.]
Wadhams, P., V. A. Squire, J. A. Ewing, and R. W. Pascal (1986), The effect of the marginal ice zone on the directional wave spectrum of the ocean, *J. Phys. Oceanogr.*, *16*, 358–376, doi:10.1175/1520-0485(1986)016<0358:TEOTMI>2.0.CO;2.
Wadhams, P., V. A. Squire, D. J. Goodman, A. M. Cowan, and S. C. Moore (1988), The attenuation rates of ocean waves in the marginal ice zone, *J. Geophys. Res.*, *93*(C6), 6799–6818, doi:10.1029/JC093iC06p06799.
Wang, R., and H. H. Shen (2010), Gravity waves propagating into an ice covered ocean: A viscoelastic model, *J. Geophys. Res.*, *115*, C06024, doi:10.1029/2009JC005591.
Weeks, W. (2010), *On Sea Ice*, 664 pp., Univ. of Alaska Press, Fairbanks, Alaska.
Wernecke, A., and L. Kaleschke (2015), Lead detection in Arctic sea ice from CryoSat-2: Quality assessment, lead area fraction and width distribution, *Cryosphere Discuss.*, *9*, 2167–2200, doi:10.5194/tcd-9-2167-2015.
Williams, T. D., L. G. Bennetts, V. A. Squire, D. Dumont, and L. Bertino (2013a), Wave-ice interactions in the marginal ice zone. part 1: Theoretical foundations, *Ocean Modell.*, *71*, 81–91, doi:10.1016/j.ocemod.2013.05.010.
Williams, T. D., L. G. Bennetts, V. A. Squire, D. Dumont, and L. Bertino (2013b), Wave-ice interactions in the marginal ice zone. Part 2: Numerical implementation and sensitivity studies along 1D transects of the ocean surface, *Ocean Modell.*, *71*, 92–101, doi:10.1016/j.ocemod.2013.05.011.
Willmes, S., and G. Heinemann (2015), Pan-Arctic lead detection from MODIS thermal infrared imagery, *Ann. Glaciol.*, *56*(69), 29–37, doi:10.3189/2015AoG69A615.
Worby, A. P., and J. C. Comiso (2004), Studies of the Antarctic sea ice edge and ice extent from satellite and ship observations, *Remote Sens. Environ.*, *92*, 98–111, doi:10.1016/j.rse.2004.05.007.
Zhang, J., R. Lindsay, A. Schweiger, and M. Steele (2013), The impact of an intense summer cyclone on 2012 Arctic sea ice retreat, *Geophys. Res. Lett.*, *40*, 720–726, doi:10.1002/grl.50190.